SANDIA REPORT
SAND2016-2870
Unlimited Release
Printed March 2016

Aerosol Deposition: Room Temperature Solid-State Deposition of Ceramics

Pylin Sarobol, Michael Chandross, Thomas D. Holmes, Andrew S. Miller, Paul G. Kotula, and Aaron C. Hall

Prepared by
Sandia National Laboratories
Albuquerque, New Mexico 87185 and Livermore, California 94550

Sandia National Laboratories is a multi-program laboratory managed and operated by Sandia Corporation,
a wholly owned subsidiary of Lockheed Martin Corporation, for the U.S. Department of Energy's
National Nuclear Security Administration under contract DE-AC04-94AL85000.

Issued by Sandia National Laboratories, operated for the United States Department of Energy by Sandia Corporation.

SAND2016-2870
Unlimited Release
Printed March 2016

Aerosol Deposition: Room Temperature Solid-State Deposition of Ceramics

Pylin Sarobol, Michael Chandross, Thomas D. Holmes, Andrew S. Miller,
Paul G. Kotula, and Aaron C. Hall.

Sandia National Laboratories
P.O. Box 5800
Albuquerque, New Mexico 87185-MS1130

Abstract

The ability to integrate ceramics with other materials has been limited by the high temperatures (>800°C) associated with ceramic processing. A novel process, known as aerosol deposition (AD), capable of preparing ceramic films at *room temperature* (RT) has been the subject of recent interest in the thermal spray and microelectronics communities. In this process, ceramic particles are accelerated using pressurized gas, impacted on a substrate and form a dense film under vacuum. This revolutionary process eliminates high temperature processing, enabling new coatings and microelectronic device integration as a back end of line process, in which ceramics can be deposited on metals, plastics, and glasses. Future impacts of this technology on Sandia's mission could include improved ceramic integration, miniaturized magnetic circulators in radar applications, new RF communication products, modification of commercial-off-the-shelf electronics, fabrication of conformal capacitors, thin batteries, glass-to-metal seals, and transparent electronics.

Currently, optimization for RT solid-state deposition of ceramics is achieved empirically and fundamental mechanisms for ceramic particle-particle bonding are not well understood. Obtaining this knowledge will allow process-microstructure-property relationship realization and will enable a differentiating ceramic integration capability. This LDRD leveraged Sandia's existing equipment and capabilities in simulation, experimentation, and materials characterization to discover the fundamental mechanisms for ceramic particle deformation, particle-substrate bonding, and particle-particle bonding in RT consolidated films. RT deformation of individual Al_2O_3 particles was examined computationally and experimentally as a model system for understanding the complex dynamics associated with *in vacuo* RT deposition conditions associated with AD. Subsequently, particle-substrate bonding and particle-particle bonding in AD Al_2O_3 consolidated films were examined computationally and experimentally. Fundamental mechanisms behind the AD process were proposed.

ACKNOWLEDGMENTS

We would like to acknowledge our collaborators—Jay D. Carrol, Brad L. Boyce, William M. Mook, Daniel C. Bufford, and Khalid Hattar—who made the work on particle deformation and our invited publication in *JTST* possible. We would like to acknowledge another set of collaborators—Nelson S. Bell, Adam W. Cook, David M. Keicher, Deidre Hirschfeld, and Paul Clem—who made our invited publication in *Ann Rev* possible.

We are grateful to Ronald C. Dykhuizen, Andrew J. Mayer, David E. Beatty, Joshua A. Hubbard, Steven Storch, Michael P. Saavedra, James F. McCloskey, Amy Allen, Bonnie B. McKenzie, Joseph A. Padilla, Adam W. Cook, and David Keicher—who helped us bring the aerosol deposition system online, characterize the films, and calculate particle velocity. We would like to thank Harlan Brown-Shaklee, Rick A. Kellogg, JÖrg Exner (University of Bayreuth), Scooter Johnson (NRL), and Edward Gorzkowski (NRL) for valuable discussions. We are in debt to Donald F. Susan, Pin Yang, and Deidre Hirschfeld for review and suggestions.

CONTENTS

FIGURES

TABLES

NOMENCLATURE

Å	Angstrom
AD	Aerosol Deposition
Al_2O_3	Alumina
°C	Degree Celsius
EDS	Energy Dispersive X-ray Spectrometry
FIB	Focused Ion Beam
Ga^+	Gallium Ion
G_C	Strain Energy Release Rate (J/m^2)
GPa	Gigapascal
J/m^2	Joules per square meter
K	Kelvin
K_{IC}	Fracture Toughness (MPa√m)
kV	Kilovolts
KVS	Kinetic Vacuum Spray
$LiCoO_2$	Lithium Cobalt Oxide
$LiMn_2O_4$	Lithium Manganese Oxide
MD	Molecular Dynamics
mm	Millimeters
mN	Millinewtons
MPa√m	Megapascal Square-root meter
m/s	Meters per Second
nm	Nanometer
nm/s	Nanometers per Second
NP	Nano Particle
NPD	Nanoparticle Deposition
ns	Nanoseconds
pJ	Picojoules
PNN	Lead Nickel Niobate
PZT	Lead Zirconium Titanate
RT	Room Temperature
RTIC	Room Temperature Impact Consolidation
RTSV	Room Temperature Spray in Vacuum
s^{-1}	Per Second
s	Second
SEM	Scanning Electron Microscopy
Si	Silicon
SNL	Sandia National Laboratories
STEM	Scanning Transmission Electron Microscopy
TEM	Transmission Electron Microscopy
XRD	X-ray Diffraction
µg/g	Micrograms per gram
µm	Micrometer
µm/min	Micrometers per Minute
µN/s	Micronewtons per Second

1. INTRODUCTION

Room Temperature deposition of metallic, ceramic, and composite materials in vacuum for electronic devices has been gaining interest and momentum. A nominal RT deposition process such as Kinetic Vacuum Spray (KVS), Room Temperature Spray in Vacuum (RTSV), Room Temperature Impact Consolidation (RTIC), aerosol type Nanoparticle Deposition (NPD), or Aerosol Deposition (AD) can be used to fabricate coatings in the solid-state. Aerosol deposition uses dry submicron sized metallic or ceramic particles suspended in carrier gas. AD relies on the pressure differential between the generation chamber and the deposition chamber (low vacuum) to generate a flow of powder carrier gas and accelerate submicron feed stock particles towards the substrate. AD also relies on submicron sized metal and ceramic particles to plastically deform and consolidate into coatings. Growth rates of 10−30 µm/min over a 1 cm^2 area have been reported, and film thicknesses up to 80 µm thick with bulk ceramic properties have been reported (1,2). Successful deposition of structural ceramics (Al_2O_3, TiO_2, AlN) (3-6), a dielectric $BaTiO_3$ (7,8), piezoelectric materials (PZT, PNN, $Bi_4Ti_3O_{12}$) (9), magnetic materials (Sm-Fe-N, Bi:YIG, YIG) (10-12), and battery cathodes ($LiMn_2O_4$, $LiCoO_2$) (2) have been demonstrated.

Particle size effects on AD coating consolidation were first reported by Akedo and Ogiso (3). Akedo and Ogiso showed 5.0 µm alumina particles fractured in compression and did not lead to consolidation in the AD process, whereas 0.5 µm alumina particles plastically deformed in compression and led to coating consolidation in the AD process. Thus, submicron particles capable of plastic deformation are used as AD feed stocks. These submicron particles travel at speeds near that of the carrier gas as the carrier gas stream exits the nozzle and expands into vacuum. As the powder carrier gas hits the substrate, it compresses and creates a densified gas layer above the substrate, known as a bow shock. The bow shock–particle interaction is reduced in vacuum, allowing small particles with low momentum to penetrate the bow shock layer, and impact the substrate with sufficient kinetic energy for deposition.

Finite element modeling has been used to investigate particle deformation and bonding (4, 13, 14). It was found that 0.3 µm alumina particles reach high pressures (2.5 GPa) and temperatures (500°C) at the particle/substrate interface during impact. However, the predicted temperatures and pressures were not high enough to cause sintering (4). During impact, the submicron particles deform, fracture, and break up into small crystallites (20−75 nm) that bind together. Dislocations, stacking faults, and amorphous phase formation from pressure induced amorphization phenomenon were observed within AD consolidated coatings (14). Molecular dynamics simulations by Imakana *et al*. showed that amorphous layers hold the key to particle-particle bonding and facilitate coating consolidation in ZnO (15). Imakana *et al*. believe that the small fragments (2 nm) in the tail of the feed stock particle size distribution create the thin amorphous layers. These small fragments impact the substrate or the previously deposited particles and become amorphized. As larger particles (submicron sized) arrive and impact the amorphized layers, they adhere and build up the coating layer-by-layer. Imakana *et al*. also showed that without the amorphized layer, arriving crystalline ZnO particles rebounded off the surface (15).

Ceramic particle consolidation in AD coatings is highly dependent on particle deformation and bonding; these behaviors are not well understood. It appears that some common mechanisms for particle deformation/bonding for different ceramics exist. In this LDRD work, RT deformation of individual Al_2O_3 particles was examined computationally and experimentally as a model system for understanding the complex dynamics associated with *in vacuo* RT deposition conditions associated with AD. Subsequently, particle-substrate bonding and particle-particle bonding in AD Al_2O_3 consolidated films were examined computationally and experimentally. Fundamental mechanisms behind the AD process were proposed.

2. OBJECTIVES AND ORGANIZATION

The objective of this LDRD was to identify fundamental mechanisms behind aerosol deposition. These mechanisms include submicron ceramic particle deformation, particle-substrate bonding, and particle-particle bonding in films consolidated at room temperature. A schematic showing an overview of this LDRD work and recommended future work is shown in Figure 1.

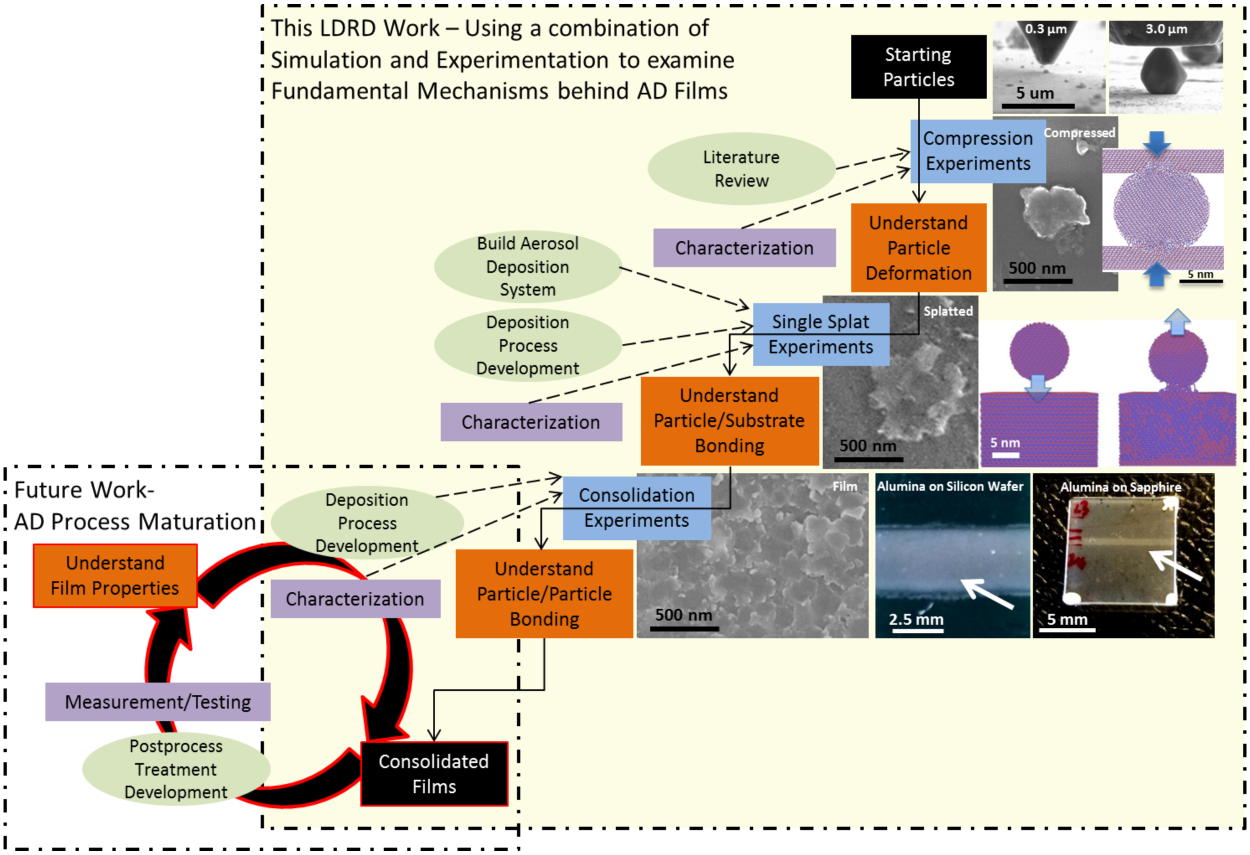

Figure 1: Schematic overview of this LDRD work: fundamental mechanisms behind AD films, proof of concept, and recommended future work (AD process maturation).

The first portion of this SAND report (Sections 3-4) addresses ceramic particle deformation. Understanding size-dependent (micron vs. submicron sized) particle deformation behavior and corresponding mechanisms is key in selecting starting feed stock particle sizes that would enable consolidation to form AD films. We utilized atomistic simulations and micro-compression experiments to observe 3.0μm and 0.3μm Al_2O_3 particles under compressive loading. The majority of this work has been presented and published in SAND2014-18127 and in an invited paper, Sarobol, P., *et al*., “Room Temperature Deformation Mechanisms of Alumina Particles Observed from In Situ Micro-compression and Atomistic Simulation,” *JTST*. Vol. 25, (2016) pp. 82-93.

The second portion of this SAND report (Sections 5-6) addresses ceramic particle deposition, particle impact on the substrate, and particle consolidation into films. We first review aerosol deposition systems and process parameters reported in literature, Section 5. The majority of this information has been published in an invited paper which contains a thorough review of the aerosol deposition process, Sarobol *et al*., “Additive Manufacturing of Hybrid Circuits,” *Ann Rev Mater Res*. Vol. 46, 2016. The information in this section was used as a basis for building SNL’s aerosol deposition system and for designing experiments aimed at understanding particle-substrate bonding and particle-particle bonding detailed in Section 6. We discuss the SNL aerosol deposition system that was constructed and brought online as part of this LDRD. We utilized SNL’s fluid-dynamics based code by Dykhuizen *et al*. to calculate 1-D particle velocity as a function of carrier gas type, chamber pressures, particle size, and nozzle geometry. These data informed deposition parameters for the single particle deposition (single splat) and consolidated film experiments reported here. In addition, we utilized atomistic simulations to understand particle-substrate interaction during impact. A manuscript on this portion of the LDRD is being prepared and will be submitted for publication.

Finally, the last portion of this SAND report (Section 7) addresses recommended future work to mature aerosol deposition technology at SNL and experiments that could be conducted to gain further knowledge of the AD process and guide future process optimization.

3. BACKGROUND ON CERAMIC PARTICLE DEFORMATION

Understanding particle consolidation or particle-particle bonding in AD first requires understanding the fundamental deformation mechanisms in sub-micron ceramic particles.

3.1. Apparent Size-Dependent Brittle-to-Ductile Transition

Bulk ceramics subjected to external loading typically exhibit brittle fracture at room temperature although plasticity may be observed at high temperatures (16-17). However, at room temperature and at the micro- and nano- length scales, substantial plasticity has been shown in ceramic single crystals. Dislocation slip was observed in compressed sapphire micro-pillars (18) and particles (4). Of relevance to AD, Akedo and Ogiso (3) showed that 5 µm Al_2O_3 particles fractured in compression, leading to coating erosion, whereas 0.5 µm Al_2O_3 particles plastically deformed under compression, resulting in coating consolidation. This apparent size-dependent brittle-to-ductile transition behavior of ceramics under external loading arises due to varying amounts of pre-exiting defects.

3.2. Role of Pre-existing Defects

Pre-existing defects of various types (e.g. mobile dislocations, stacking faults, twins, internal boundaries, cracks, etc.) and densities are commonly found in metallic and ceramic materials. These defects lead to diverse deformation behaviors observed in compressed metallic and ceramic materials, and are especially important with decreasing size (e.g. micro-pillars and particles) (18-27).

Montagne *et al*. (18) performed room-temperature micro-pillar compression experiments on differently oriented, 1 µm diameter by 3 µm high, Al_2O_3 single crystals. They observed that deformation behavior of these micro-pillars consistently fit into two categories. In the first category, the micro-pillars exhibited consistent and *high* uniaxial stress at the load drop, as well as visible slip planes. Depending on orientation, both visible slip planes and cracks were observed. In the second category, the micro-pillars exhibited inconsistent and *lower* uniaxial stress at the load drop, as well as cracks. Montagne *et al*. hypothesized that micro-pillars in the first category were initially defect-free whereas the micro-pillars in the second category contained pre-existing defects based on statistical distributions. Based on their hypothesis, Montagne *et al*. proposed two governing mechanisms for the observed deformation behaviors of the differently oriented compressed pillars—plasticity and fracture (18). Deformation of initially defect-free pillars was governed by plasticity—heterogeneous dislocation nucleation and glide. Deformation of pillars with pre-existing defects was governed by fracture—crack nucleation and propagation (18).

4. CERAMIC PARTICLE DEFORMATION

The work in this section was in collaboration with Jay D. Carrol, Brad L. Boyce, William M. Mook, Daniel C. Bufford, and Khalid Hattar and was published (28).

4.1. Hypothesis on Particle Deformation Mechanisms

Statistical distributions of pre-existing defects scale with size. Larger ceramic particles contain higher numbers of pre-existing defects than smaller ceramic particles. We hypothesize the following deformation mechanisms for differently sized ceramic particles in compression;

> (i) in nanoscale (tens of nm diameter) ceramic particles (without pre-existing defects or dislocations), deformation is governed by plasticity, and can accommodate a higher strain energy (SE) per unit volume associated with dislocation nucleation and slip;
> (ii) in large (several micron diameter and above) ceramic particles (with many initial flaws and defects, including high numbers of immobile dislocations), deformation is governed by fracture, and can accommodate a lower SE per unit volume before crack initiation and propagation;
> (iii) in small (hundreds of nm diameter) particles, (with some initial immobile dislocations), a combination of fracture and plasticity governs deformation. This leads to more experimental scatter where particles can accommodate intermediate SE per unit volume before dislocation nucleation and slip preceding crack nucleation and propagation." (28).

Here we use a combination of methods to elucidate the mechanisms responsible for the observed size-dependent deformation behavior in nano, sub-micron, and micron sized α-Al_2O_3 particles under compression. Atomistic simulations were used to test hypothesis (i), while in situ particle micro-compression experiments conducted in a scanning electron microscope (SEM) and a transmission electron microscope (TEM) were used to test hypotheses (ii) and (iii) (28).

4.2. Pre-existing Defects in Particles

We obtained high purity α-Al_2O_3 particles with nominal sizes of 3.0 µm and 0.3 µm from Sumitomo Chemical Co., LTD. XRD examination confirmed both sets of particles were corundum, α-Al_2O_3. We examined particle morphology and size in the SEM. Particle size distributions were reported in SAND2014-18127. We examined the particle interiors using the TEM. The 0.3 µm Al_2O_3 particles (electron transparent) were dispersed onto a carbon-coated copper TEM grid. The 3.0 µm particles were cross-sectioned using a focused ion beam (FIB) and prepared for subsequent *in situ* lift-out for TEM imaging. An FEI Company Tecnai F30-ST TEM/STEM operated at 300 kV and an FEI Company Titan G2-80-200 operated at 200 kV were used for imaging (28). The latter instrument is equipped with a spherical aberration corrector on the probe forming optics and is capable of resolving sub-angstrom features.

It was found that the 0.3 µm particles were largely defect-free; although, they contained some amount of pre-existing dislocations (Figure 2a,b). On the other hand, the 3.0 µm particles contained many defects including a low-angle grain boundary (GB) (Figure 3a) or many dislocations and stacking faults (Figure 3b). We hypothesized that pre-existing defects and dislocations in these particles were likely immobile and introduced during particle precipitation. These pre-existing defects highly influence particle responses during compression at the small length scales (28).

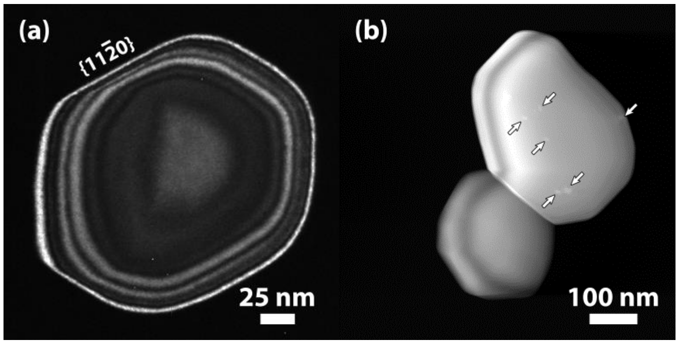

Figure 2: TEM images from (a) a largely defect-free 0.3 µm particle (looking down the basal plane normal) and 9b) two particles sharing a sintered boundary containing dislocations (arrows) (28).

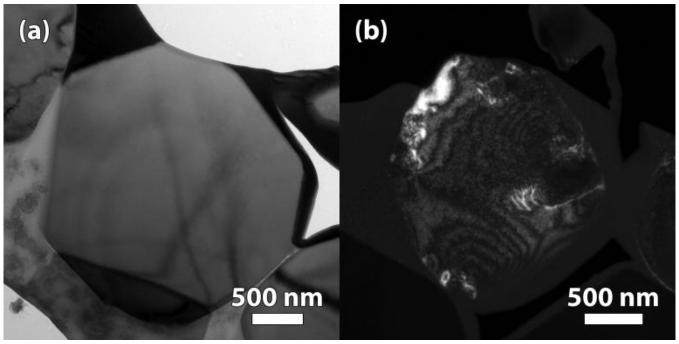

Figure 3: TEM images from (a) a largely dislocation-free 3.0 µm particle with a low angle grain boundary and (b) a highly defective single-crystalline 3.0 µm particle with numerous dislocations and stacking faults (28).

4.3. Simulated Micro-Compression of 10 nm Particles

4.3.1. Methods and Assumptions

Molecular dynamics (MD) allows identification of dislocations, slip planes, and particle fracture. In this study, a force-field (FF) for ceramics developed by Garofalini (29) was used (Large-scale Atomic/Molecular Massively Parallel Simulator, LAMMPS). This FF accurately predicted surface structures, defect concentrations, and intergranular film composition in a variety of ceramics. Fracture surfaces have been studied with this FF (30), although fracture and plasticity have not. Computational limitations restricted our MD simulations to particle diameters < 50 nm (~36 million atoms). To circumvent this size limitation, we used the hypothesis that ‘smaller’ particles (< 1 µm) are nearly defect-free, and ‘larger’ particles (> 1 µm) contain initial immobile dislocations or a grain boundary (GB). We simulated two similarly sized 10 nm (~300,000 atoms) nanoparticles (NPs) that were either a single crystal or a bicrystal. We postulated that, in compression, the single crystal NP will accommodate higher SE and show dislocation plasticity, whereas the bicrystal NP, will accommodate lower SE and fracture. This approach enables us to study NP response to compression in computationally-feasible systems (28).

Spherical NPs were created from an initial bulk single crystal α-Al_2O_3 with the basal plane {0001} oriented perpendicular to the compression direction. The single crystal NP was created by removing all atoms that did not lie within a 5 nm prescribed radius from the NP center. The bicrystal NP was created by duplicating the single crystal NP and given a known rotation along the three Euler angles (Bunge convention). The initial and rotated NPs were both cut in half along the XZ-plane and joined at the center. The NPs were energy minimized at 0 K, followed by equilibration at RT for 1 ns. Both the single crystal and bicrystal NPs were compressed between two single crystal α-Al_2O_3 walls at a constant velocity of 20 m/s. Particles were compressed by ~1/3 of the initial particle diameter, and potential energy, force, and stress as a function of separation were calculated (28).

4.3.2. Single Crystal, 10nm Al_2O_3 Particle Response to Compression

The compressed single crystal particle clearly exhibited plastic deformation (Figure 4). Primary and secondary dislocations nucleated from the Al_2O_3 wall/NP contact points. The primary dislocations first nucleated and then moved through the NP (Figure 4B) on rhombohedral planes (Figure 4C). Then, the secondary dislocations moved inward from the particle surface and terminated at the primary dislocations (Figure 4D) (28).

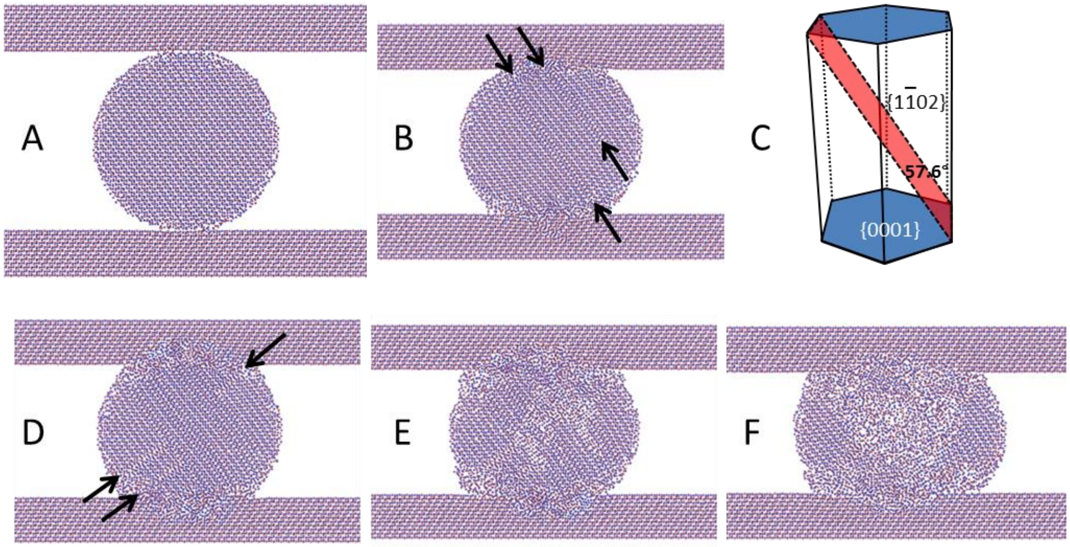

Figure 4: Thin slices through a 10 nm single crystal NP, showing atom positions at different stages of compression. (a) at first contact. (b) immediately after the primary dislocations nucleated at the top contact plane and moved through the particle (arrowed). (c) The 57.6° angle between slip planes and basal planes suggested that slip planes were rhombohedral,. (d) Secondary dislocations nucleated and moved from the particle surface inward, terminating at the primary dislocations. (e) Void nucleation. (f) Particle fracture and separation. Figure taken from (28).

Note that the rhombohedral plane was one of the reported common slip planes in Al_2O_3 (31-35). Subsequently, void nucleation was observed (Figure 4E) and the NP fractured, separating into segments (Figure 4F). Some areas in the fractured NP appeared crystalline with different orientations, while other areas appeared amorphized (Figure 4E) (28).

4.3.3. Bicrystal, 10 nm Al_2O_3 Particle Response to Compression

The Bicrystal NP also plastically deformed but did so differently than the single crystal NP. It appeared, in the first stage of the Bicrystal NP deformation that the atoms from the left and right halves of the NP moved into the GB (Figure 5B,C) at the wall/NP contact point. With further compression, void nucleation occurred at the GB and the bicrystal NP fractured (Figure 5D,E). No dislocation nucleation or movement was observed in the bicrystal NP. Similar to the single crystal NP, some areas in the fractured Bicrystal NP appear crystalline with different orientations, while others appear amorphized (Figure 5E) (28).

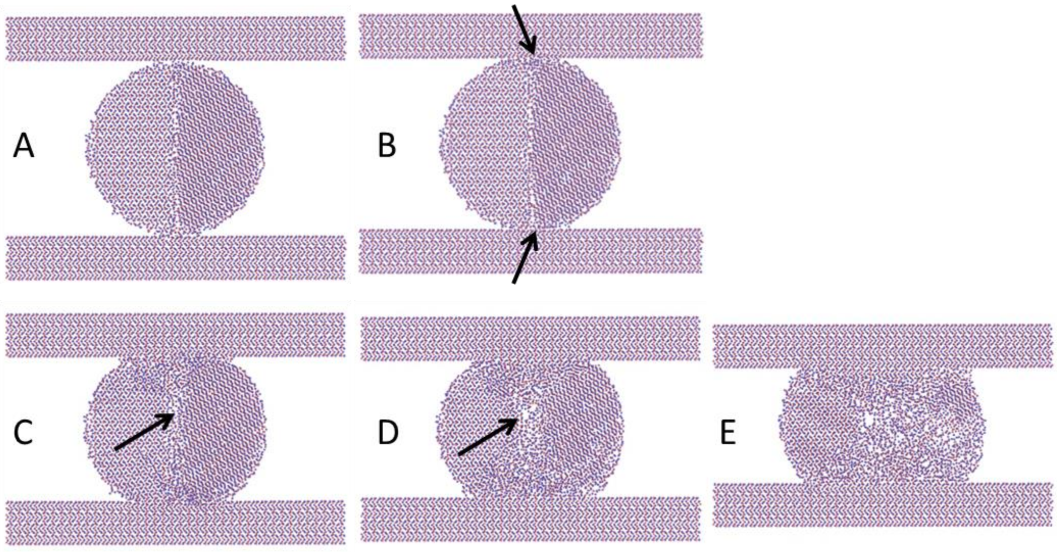

Figure 5: Thin slices through a 10 nm bicrystal NP, showing atom positions at different stages of compression. The left side of the bicrystal NP has the {0001} plane perpendicular to the compression direction. The right side of the bicrystal NP is randomly rotated. (a) Moment at first contact; (b) Atoms from the particle surface at the contact points moved down the grain boundary (arrowed); (c) Moment before void nucleation; (d) Void nucleation at the grain boundary (arrowed); (e) Particle fracture and separation. Figure taken from (28).

4.3.4. Absorbed Strain Energy

Force vs. compression distance was calculated for both NPs and is shown in Figure 6. Generally, the forces increased as compression distance increased, reached a maximum, and then dropped. The large force drop associated with compressed volume cracking in our simulated compressed single crystal NP appeared similar to force drops reported in other micro-compression experiments. The peak force in a single crystal NP was substantially higher than that in the bicrystal NP. In addition, the absorbed strain energy (SE, calculated by integrating the force vs. displacement curve up to the peak value, marked 'X') was higher for the single crystal NP by a factor of 2.9 (28). The calculated compression ratio (particle initial height divided by final height) prior to the force drop was also found to be higher for the single crystal NP by a factor of 1.5 (28). The authors associate high SE with dislocation plasticity—mobile dislocation nucleation and movement—in the initially defect-free, single crystal NP. From this result, it becomes clear that mobile dislocations are needed to initiate plastic deformation prior to fracture. In contrast, an immobile defect—a GB—will act as a void nucleation site, providing no dislocation plasticity prior to particle fracture (28).

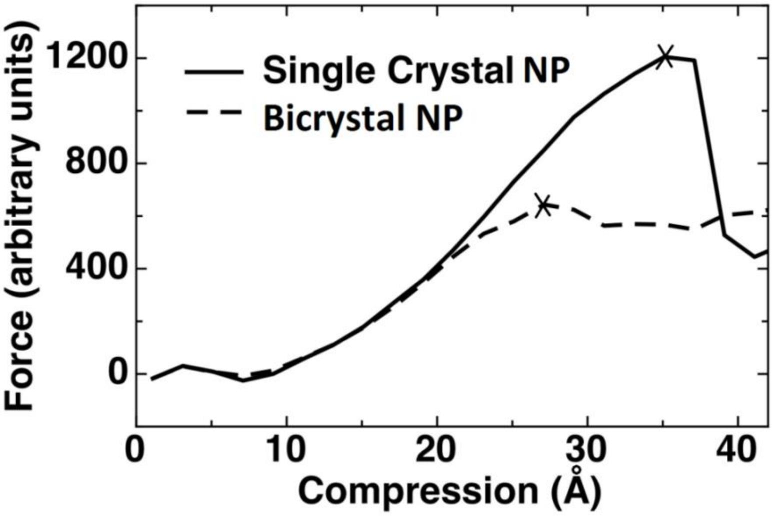

Figure 6: Force vs. displacement (Angstrom) for the 10 nm diameter NPs—a single crystalline NP with no defects (solid curve) and the bicrystal NP with a grain boundary as an immobile defect (dashed curve). The "X" on each curve marks the fracture point. Figure taken from (28).

4.4. Experimental Micro-compression of 0.3µm & 3.0µm Al_2O_3 Particles

Micro-compression in the SEM was performed on both the 0.3 µm and 3 µm Al_2O_3 particles. The particles were suspended in ethanol and drop cast onto {0001} sapphire substrates. The compression axis was perpendicular to the {0001} sapphire substrate surface. The imaging axis was at 86° relative to the compression axis so that the indentation process could be observed in situ. The Zeiss Supra 55VP field emission gun SEM was operated at 5.0 kV. All particle loading was performed using a Hysitron PI85 SEM Picoindenter (36) in displacement control mode. A 3 µm diameter boron-doped diamond flat punch tip moving at a nominal 15 nm/s was used to compress the 0.3 µm particles, whereas a 6 µm diameter flat punch tip moving at a nominal 150 nm/s was used to compress the 3 µm particles (see Table 1 for actual values) . Compression rates (calculated as the displacement rate divided by the initial particle diameter) of 0.05 s^{-1} and 0.005 s^{-1} were used for the small and large particles, respectively (28).

Micro-compression in the TEM was performed only on the electron transparent 0.3 µm particles. All TEM compression testing used an in situ Hysitron PI95 TEM Picoindenter with a 1 µm diameter boron-doped diamond flat punch tip, and was performed in a JEOL 2100 LaB_6 TEM at 200 kV and imaged in bright-field mode. Compression was performed in open loop mode with a loading rate of 10 µN/s (corresponding to a displacement rate of ~2 nm/s and compression rates of ~0.007s^{-1}). Small particle response was observed in situ (28).

4.4.1. Submicron-sized, 0.3μm Al_2O_3 Particle Response to Compression

Particle compression in the SEM revealed that the 0.3 μm diameter "small" Al_2O_3 particles, which contained very few pre-existing dislocations, exhibited a range of responses to compression, including significant *plastic deformation, shape change, and cracking without fragmentation* (Figure 7). Moreover, particle compression in the TEM revealed that the 0.3μm diameter "small" particles exhibited dislocation nucleation/movement during compression and *orientation spread (mosaicity)* after compression (Figure 8) (28).

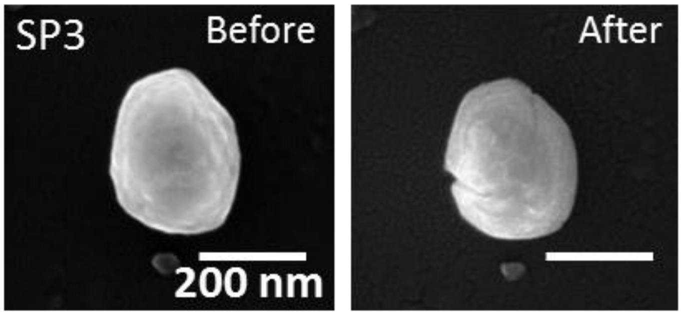

Figure 7: Typical SEM images before and after compression of a 0.3 μm alumina particle. The small 0.3 μm particle, SP3, changed shape and cracked in compression, but stayed mostly intact.

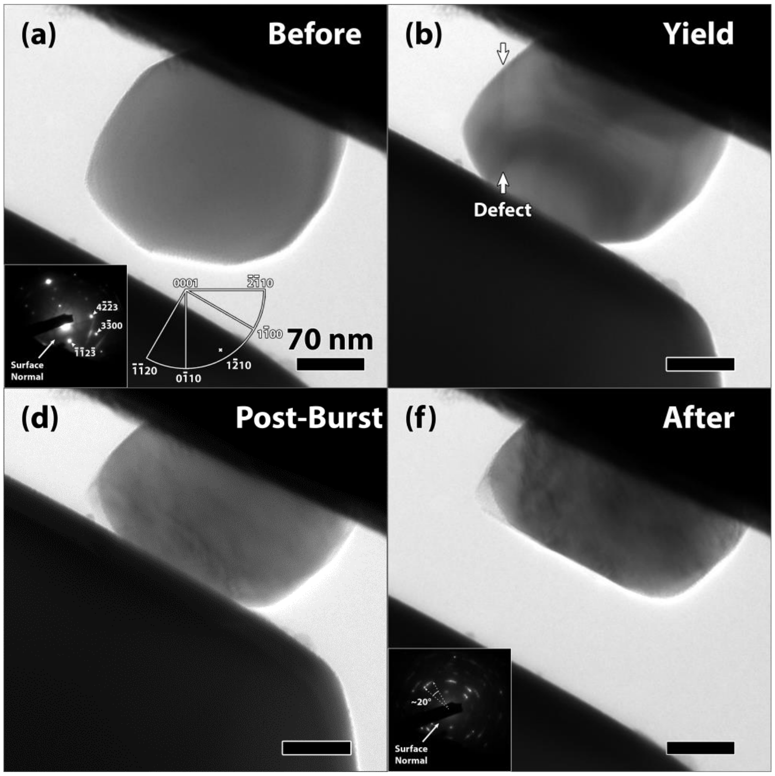

Figure 8: TEM micrographs and SAD patterns, with snapshots taken during compression. (a) Initial overview, with inset SAD pattern showing a single crystal structure with zone axis near $\{\bar{9}\,\bar{9}\,18\,6\}$. (b) moments after the first observable defect appeared (d) moments after fracture. The post-compression SAD pattern (f) reveals a polycrystalline structure with ~20° orientation spread (mosaicity). Post-compression SEM examination showed this particle cracked but did not fragment.

4.4.2. Micron-sized, 3.0µm Al_2O_3 Particles Response to Compression

Particle compression in the SEM revealed that the 3.0 µm "large" diameter Al_2O_3 particles, which contained higher numbers of pre-existing dislocations or GBs, exhibited *brittle fracture and fragmentation* (Figure 9) (28).

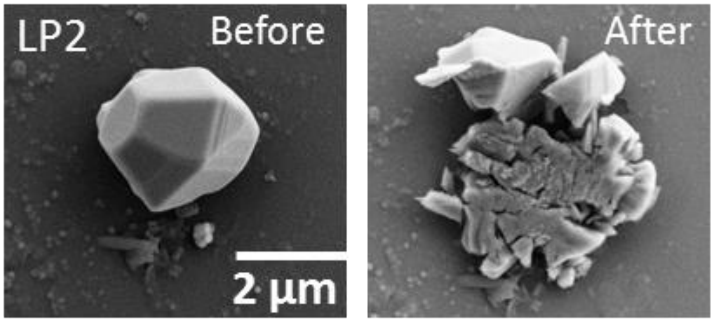

Figure 9: Typical SEM images before and after compression of a 3.0 µm alumina particle. The large 3.0 µm particle, LP2, exhibited cleaving (characteristic of brittle fracture), fracture, and fragmentation.

4.4.3. Absorbed Strain Energy

The load vs displacement curves from micro-compression in the SEM as well as images taken before and after compression for four small (0.3 µm) particles (designated as "SP's") are shown in Figure 10 and those for four large (3.0 µm) particles (designated as "LP's") are shown in Figure 11. It was difficult to determine the exact transition from the elastic regime to the plastic regime. Generally, the load initially increased rapidly with increasing displacement. Initial load vs. displacement curves for small particles appeared wavy with many small perturbations. These perturbations (displacement bursts) were not observed in the curves for large particles, even when they were plotted on a similar scale (28). These small displacement bursts in compressed small particles suggested dislocation avalanches. At some critical load, both small and large particle curves exhibited a displacement burst (i.e. a large displacement gain at a relatively constant load) when the particle fractured/collapsed. Finally, the load dropped due to tip retraction and the control system recovered (28).

The load vs displacement curves from micro-compression in the TEM as well as images taken before and after compression for two small (0.3 µm) particles (designated as "TEM-SP's") are shown in Figure 12 (28). Note that we cannot directly compare the apparent shape of the curves from the SEM operating in displacement-control mode (Figure 10) and the TEM (Figure 12) operating in open loop mode. However, we can compare the particle size, compression rate, and corresponding volumetric strain energy density (VSED), areal strain energy density (ASED), and compression ratio at fracture, of all particles (28). These are summarized in Table 1.

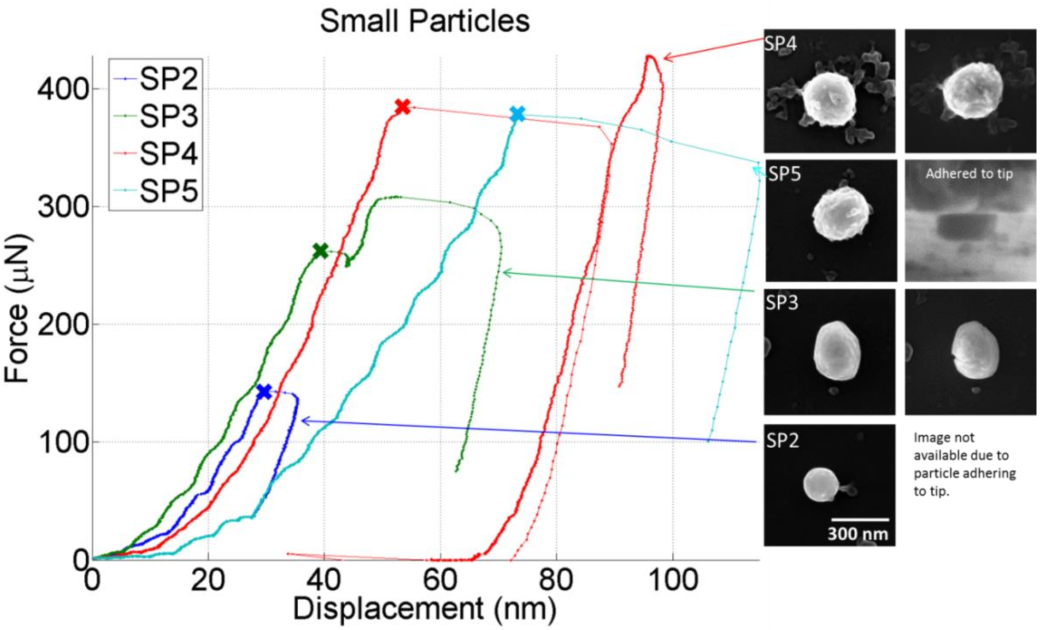

Figure 10: Load vs. displacement curves using a Hysitron PI85 SEM Picoindenter in the displacement control mode and SEM images before and after loading for four 0.3 μm particles (SP2-SP5). Waviness in the curve is associated with dislocation avalanche. The "X" on each curve marks the first fracture event for each particle. Figure taken from (28).

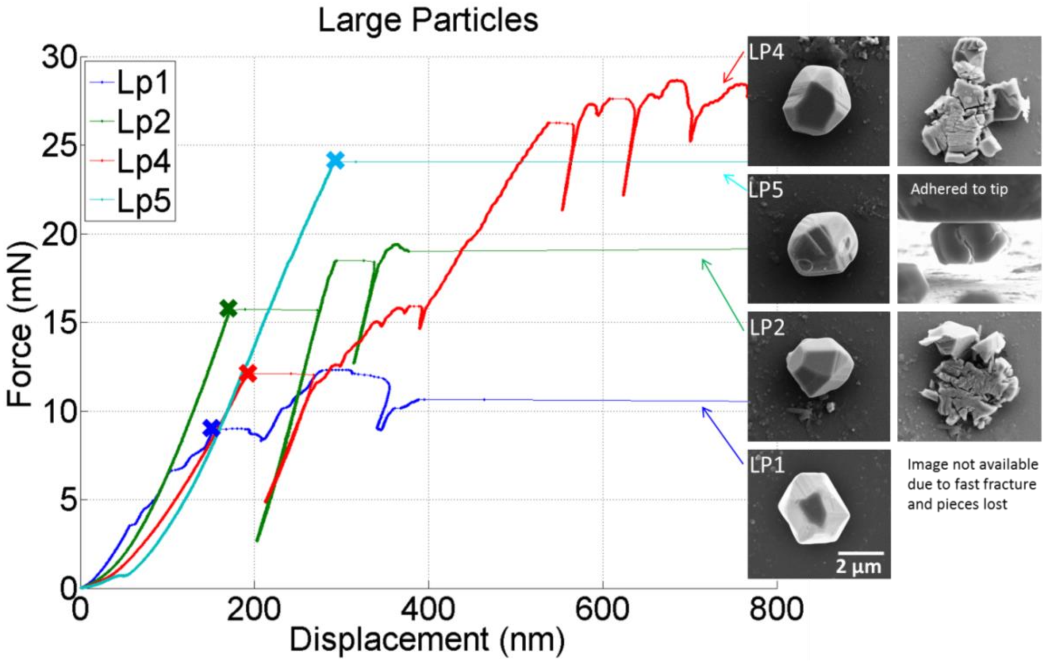

Figure 11: Load vs. displacement curves using a Hysitron PI85 SEM Picoindenter in the displacement control mode as well as SEM images before and after loading for four 3 μm particles (LP1, LP2, LP4, and LP5). The "X" on each curve marks the first fracture event for each particle. Figure taken from (28).

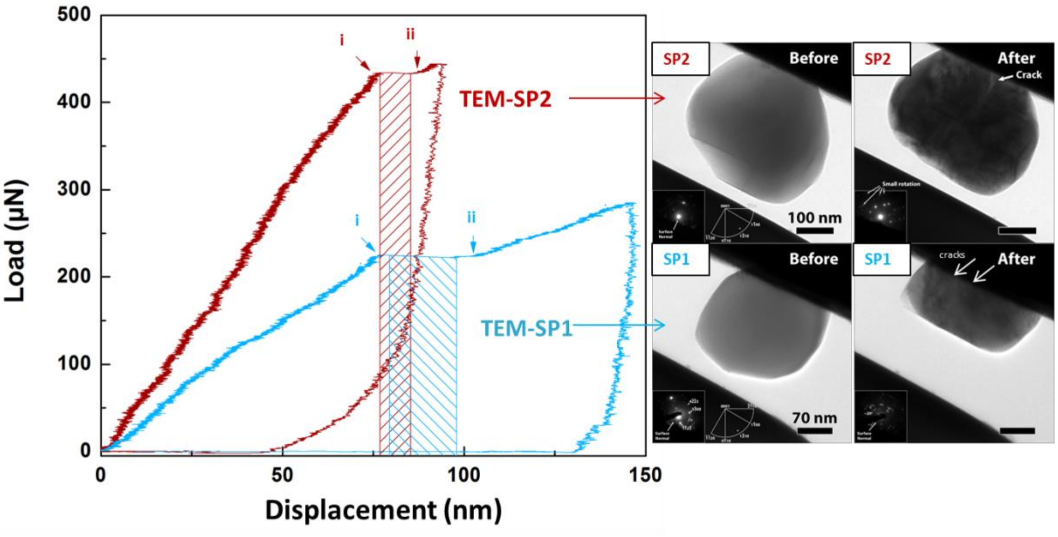

Figure 12: Load vs. displacement curves using a Hysitron PI95 TEM Picoindenter in the open loop mode and TEM images before and after loading for two 0.3 µm particles (TEM-SP1 and TEM-SP2). Section i-ii marked the displacement excursion corresponding to particle fracture.

Table 1: Diameter, compression rate, as well as corresponding VSED, ASED, and compression ratio at fracture for all particles compressed in the SEM and the TEM. Table taken from (28).

Particle Identifier	**Diameter (µm)**	**Compression Rate (s^{-1})**	**Volumetric Strain Energy Density (VSED) at fracture (MJ/m^3)**	**Areal Strain Energy Density (ASED) at fracture (J/m^2)**	**Compression Ratio at fracture (%)**
Large Particles					
SEM-LP1	2.9	0.03	47	45	5
SEM-LP2	2.6	0.006	106	92	5
SEM-LP4	2.9	0.005	70	67	5
SEM-LP5	2.9	0.003	203	196	7
Avg Large Particles	**2.8**	**-**	**106±69**	**100±67**	**5.5 ± 1**
Small Particles					
SEM-SP2	0.17	0.09	494	28	11
SEM-SP3	0.29	0.05	366	35	12
SEM-SP4	0.28	0.05	607	57	13
SEM-SP5	0.29	0.05	675	65	16
TEM-SP2	0.38	0.005	573	73	32
TEM-SP1	0.24	0.009	1066	83	27
Avg Small Particles	**0.26**	**-**	**630±238**	**57±21**	**18 ± 9**

The apparent SE at fracture was estimated by integrating under the load vs. displacement curve up to the first fracture event (marked ‘X’). Assuming that each particle is spherical, the VSED is calculated by normalizing the apparent SE at fracture by the particle volume. VSED at fracture represents the accommodated SED associated with dislocation activity throughout the volume. Assuming each particle experienced a through-particle fracture and that two new fracture surfaces were created, the ASED is calculated by normalizing the apparent SE at fracture with twice the particle cross-sectional area. ASED at fracture approximates the material’s (i.e. Al_2O_3) resistance to fracture, similar to toughness (28). The two different SED’s measure two distinct phenomena: VSED is a measure of plasticity, dislocation activity, and fracture, which consume energy throughout the material volume; on the other hand, ASED is a measure of fracture toughness because the fracture process involves transferring energy into new fracture surfaces (28). Finally, the compression ratio at fracture was calculated by normalizing the total displacement with the initial particle diameter.

The VSED at fracture varied due to different amounts of pre-existing (and likely immobile) dislocations or other defects in the particles and different loading orientations (28). The average VSED at fracture for the small particles was 630 ± 238 MJ/m^3 – six times higher than that for the large particle average, 106 ± 69 MJ/m^3. It is hypothesized that the higher VSED was associated with dislocation nucleation/movement in the small particles, as predicted by simulation and evidenced by waviness of the load vs. displacement curve (28). The significantly higher VSED measured in small particles indicates they can accumulate more plasticity before fracture (28).

The ASED at fracture was found to be relatively independent of particle size. The ASED values reported in Table 1 (28–196 J/m^2 or 35–92 J/m^2 excluding two outliers) are near the calculated range of orientation-dependent crystal strain energy release rate (i.e. a value indicating the ‘toughness’) of single crystal alumina, which is 16 J/m^2 to 65 J/m^2 (37). As previously shown, there are multiple fractures for the large particles. If these fractures occurred simultaneously, the resulting ASED values would be even lower than reported in Table 1 and closer to the small particle values and the reported values (37). The close agreement in ASED for small and large particles indicates that it is a materials property that is relatively size-independent. It also suggests that the electron beam induced plasticity phenomenon likely did not occur during our micro-compression experiments (28).

The average compression ratio at fracture of small particles was 18 ± 9%, over twice that of the large particles, 5.5 ± 1%. Fast fracture/fragmentation of the 3 μm large particles was observed *in situ* during compression in the SEM. Similarly-sized particles were reported *not* to consolidate in AD process (3), suggesting a lack of particle plasticity and bonding. The kinetic energy density for small and large particles traveling at 200-600 m/s during AD process is estimated to be 79-711 MJ/m^3. Assuming very little kinetic energy is converted to heat, as most kinetic energy is converted to SE absorbed during impact, we suspect that large particles traveling at >233 m/s would fracture (28). In contrast, small particles traveling at <565 m/s would accommodate high enough SE associated with dislocation plasticity (without fracture), providing consolidation. Accordingly, one would hypothesize that small particles traveling at >565 m/s would fracture during impact, likely resulting in poor coating consolidation (28).

4.5. Proposed Ceramic Particle Deformation Mechanisms

It is important to note several major differences between the simulation and experiments reported here. All simulations were performed at a high displacement rate (20 m/s) on very small (10 nm) Al_2O_3 NPs; giving a compression rate ~ $2x10^9$ s^{-1}. In contrast, experimental in situ micro-compression in the SEM and the TEM performed on real 3 μm and 0.3 μm, Al_2O_3 particles used much lower displacement rates (~2-150 nm/s). Despite these differences, both the simulation and the experimental results supported the proposed deformation mechanisms for compression behavior in differently sized ceramic particles and suggested deformable sub-micron particles are building blocks of AD ceramic films (28).

Both the simulation and micro-compression results agree qualitatively. They show that compressed initially, relatively defect-free ('small') particles undergo significant plastic deformation/shape change prior to fracture whereas highly defective ('large') particles undergo fast fracture and fragmentation. Experiments showed the average compression ratio before fracture of the small particles was 3 times that of the large particles. Similarly, simulation showed the compression ratio before fracture of the defect-free single crystal NP was 1.5 times that of the bicrystal NP (28). Additionally, both results show that higher VSED are associated with dislocation nucleation/motion (plastic deformation) of small ceramic particles that were initially relatively defect-free. In contrast, particles with an initial GB as an immobile defect built up less VSED before fracture (28). Specifically, experimental results showed the average VSED before fracture for the small particles was 6 times that of the large particles. Likewise, simulation results showed the average absorbed energy prior to fracture for the defect-free NP was 3 times that of the bicrystal NP. Moreover, both the simulation and in situ TEM micro-compression results showed dislocation nucleation/motion and separation into small crystallites. The VSED ratio of 6, between small and large particles, from experiments (compared to 2.9 from the simulations) is likely due to displacement rate effects (nm/s vs. m/s) and forcing a single defect in bicrystal simulations as opposed to multiple defects in the actual large particles (28). Presence of stress concentrators (facets/cracks) also contributed to the compression ratio being much smaller in the experiments than in the perfectly spherical simulated NPs (28).

Several implications for AD emerged from this work. First, plastic deformation, shape change, orientation spread (mosaicity), and fracture without fragmentation are possible in sub-micron sized ceramic particles (28). These mechanisms contribute to coating buildup in AD. Sub-micron sized ceramic particles are capable of RT plastic deformation at low compression rate (as shown in this work) and high compression rates as reported in the literature (2). Second, the use of sub-micron sized particles that contain pre-existing mobile dislocations (as opposed to dislocation-free particles or particles with immobile dislocations) will accommodate additional low VSED (corresponding to lower particle velocity in AD) with further deformation and will likely lead to higher deposition efficiency in AD (28). This is due to a lower VSED associated with moving the pre-existing mobile dislocations (as opposed to nucleating new dislocations) during the plastic deformation process (28). Pre-existing mobile dislocations could be introduced into particles via feed stock ball milling. Future work beyond the scope of this LDRD that further explores the effects of particle size, presence of mobile dislocations, crystal orientation, and strain rate on the observed particle deformation behavior, would provide valuable insights. Third, particles even smaller than 0.3 μm would also be expected to be relatively defect-free and able to deform plastically; however, their smaller size would mean lower impact energy in AD (due to lower mass). Consequently, AD of ceramics involves a compromise between plastic deformation, particle size, and impact energy (28).

4.6. Key Points from Particle Compression Studies

Pre-existing defects play an important role in the deformation behavior of nano-, sub-micron, and micron sized alumina particles in compression. Atomistic simulations of defect-free alumina nanoparticles showed that nucleation and movement of mobile dislocations occurred during compression and was accompanied by significant plastic deformation. This finding supports the idea of plasticity-governed deformation, in which nucleation/glide of dislocations control deformation of small particles (28). Simulated compression of a nanoparticle with an internal boundary as a pre-existing immobile defect did *not* result in dislocation plasticity. The findings from atomistic simulations are in good qualitative agreement with those from *in situ* micro-compression experiments (28). Relatively defect-free sub-micron alumina particles can accommodate high volumetric strain energy density associated with dislocation nucleation/motion (significant plastic deformation and shape change) when loaded in compression. These particles fractured but did not fragment. Micron-sized alumina particles, typically with large numbers of defects or a grain boundary only accommodated low volumetric strain energy density before fracture and fragmentation when loaded in compression (28). Implications from these LDRD studies gave insights into particle size selection for the aerosol deposition experiments reported below. They also help understand mechanisms behind the use of ball-milling to increase the efficiency of room temperature consolidation in aerosol deposited ceramic films, discussed in Section 5.2 (28).

5. BACKGROUND ON AEROSOL DEPOSITION PROCESS

In a nutshell, AD uses dry submicron sized metallic or ceramic particles suspended in carrier gas and relies on the pressure differential between the aerosol generation chamber and the spray deposition chamber (low vacuum) to generate flow of carrier gas, accelerating the submicron particles towards the substrate. This section reviews literature reported aerosol deposition systems and pertinent process parameters. We have published an invited paper containing a thorough review of the aerosol deposition process, Sarobol *et al*., "Additive Manufacturing of Hybrid Circuits," *Ann Rev Mater Res*. Vol. 46, 2016 (38). The information in this section was used as a basis for building SNL's aerosol deposition system and for designing experiments aimed at understanding particle-substrate bonding and particle-particle bonding detailed in Section 6.

5.1. Aerosol Deposition System Design

A schematic diagram of a typical aerosol deposition system as reported by Akedo (4) is shown in Figure 13. Gas travels from the source to the aerosol chamber, where it "bubbles" through the particle bed on a filter and carriers suspended particles towards the deposition nozzle, located in a low pressure deposition chamber. The low pressure deposition chamber is needed to minimize the "bow shock" effect created by carrier gas recompressing on the substrate. Minimizing the bow shock allows submicron particles to reach the substrate with sufficient kinetic energy for deposition.

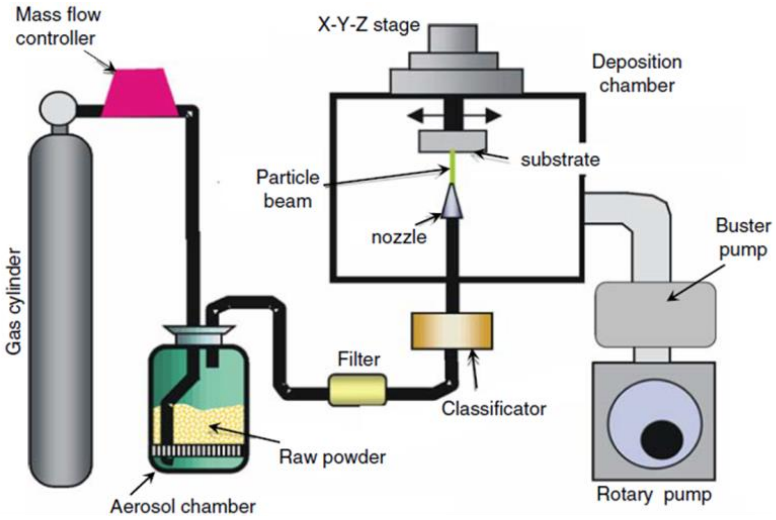

Figure 13: Schematic of an aerosol deposition system from Akedo (4).

The carrier gas speed is dictated by the pressure differential between the aerosol generation chamber and the deposition chamber (mild to medium vacuum). Moreover, the deposition nozzle geometry can be designed to allow further acceleration of the carrier gas and the suspended particles. The nozzle design is critical to successful aerosol deposition and information regarding nozzle design is scarce in the open literature. A paper by Chun et al. (13) was one of the few that discussed nozzle geometries and provided schematics of an AD nozzle. We used their nozzle design as a basis and modified it for our AD system at SNL (details in Section 6.1).

The nozzle is positioned under the substrate and the particle stream is directed upward towards the substrate. We speculated that the purpose of this configuration is to minimize entrained fragments in the coatings as the impacted particles that did not “stick” fall away due to gravity.

Relevant reported deposition parameters for various materials, using different carrier gases and pressures, are shown in Table 2. The effect of these parameters on particle velocity, deposition efficiency, and the resulting consolidated AD coatings are discussed in the next section. We used information in this table to help guide our process parameter selection for the deposition experiments discussed in Section 6.3 and 6.4.

Table 2: Reported Aerosol Deposition Parameters from Literature

Materials	Staring Powder Size (µm)	Powder Preparation	Final powder size (µm)	Carrier Gas	Carrier Gas Flow		Aerosol Generation Chamber Pressure (psi)	Deposition Chamber Pressure (mtorr)	Traverse Speed (mm/s)	Stand off (mm)	Ref
					Low (L/min)	High (L/min)					
Al2O3	0.3	80g powder in chamber, 20 passes		He	2	18			1		1
Al2O3	0.5	4 hrs in cyclohexane, dry at 120C , sieved through 90um screen, dry at 200C		100%N2, 100%O2, 100%He, or in between	6		3.63	7500	1	3	2
Al2O3	0.1-0.3			Air compresser pressure 0.4 Mpa	20	30	58	150000-300000	0.05, 0.15, 0.2	3	3
Al2O3	0.5			Air compresser pressure <1 Mpa, under low vacuum >3.3 kpa			58	300000		1, 3, 5, 7	4
Al2O3	0.2-0.5			He, N2, air	1-4	10	1.45-11.6	375-2250	0.125-10	1-40	5
Al2O3, PZT, AlN, MgB2	0.2-0.5		0.3-2.0	He, N2, air	1	10	1.45-11.6	375-2250	0.125-10	1-40	6
Bi:YIG		100 rpm/10 hrs in IPA, anneal at 1000C for 1 hr, ball mill	0.1-0.5	N2	0.5	10		7.5-30			7
Sm-Fe-N	3			He	1	10	1.16-8.7	150-750		1-20	8
Sm-Fe-N	3			He	6					10	9
PZT, PLZT				O2				<150 before flow, 4,500 during dep			10
BaSrTiO3	0.6			O2	4	7		2250-6000	1.2	10-35	11
BaTiO3-Ag	0.5 BaTiO3, 0.2-0.5 Ag			O3	4			7500			12
PZT				O2	4			7500			13

References for Table 2.

1 P. Hyungkwon *et al.*, "Shock-induced Plasticity and Fragmentation Phenomena during Alumina Deposition in the Vacuum Kinetic Spraying Process," *Scripta Mater*. **100** (2015) 44-4.

2 M. Schubert *et al.*, "Influence of Carrier Gas Composition on the Stress of Al_2O_3 Coatings Prepared by the Aerosol Deposition Method," *Materials* **7** (2014) 5633-5642.

3 D.M. Chun and S.H. Ahn, "Deposition Mechanism of Dry Sprayed Ceramic Particles at Room Temperature Using a Nano-Particle Deposition System," *Acta Mater* 59 (2011) 2693-270.

4 D.M. Chun *et al.*, "Effect of Stand-off Distance for Cold Gas Spraying of Fine Ceramic Particles (<5 µm) under Low Vacuum and Room Temperature using Nano-Particle Deposition System (NPDS)," *Surface and Coatings Technology* **206** (2012) 2125-2132.

5 J. Akedo and H. Ogiso, "Room Temperature Impact Consolidation (RTIC) of Ceramic Fine Powder on Aerosol Deposition

6 J. Akedo, "Aerosol Deposition Method for Fabrication of Nano Crystal Ceramic Layer Novel Ceramics Coating with Collision of Fine Powder at Room Temperature," *Materials Science Forum* **449-452** (2004) 43-48.

7 M. Inoue *et al*., "Preparation of Thick Magnetic Garnet Films with Aerosol Deposition Method and Their Magnetic Properties," *Proceedings of the IMAPS/ACerS International conference and Exhibition on Ceramic Interconnect and Ceramic Microsystems Technologies*, April 24-27, 2006, Denver, CO.

8 S. Sugimoto *et al*., "Magnetic Properties of Sm-Fe-N Thick Film Magnets Prepared by the Aerosol Deposition Method," *IEEE Trans Magnetics,* **39** (2003) 2986-2988.

9 S. Sugimoto *et al*., "Effect of Applied Field during Aerosol Deposition on the Anisotropy of Sm-Fe-N Thick Films," *J. Magnetism Magnetic Mater*, **290-291** (2005) 1202-1205.

10 M. Nakada *et al*., "Aerosol Deposition Fabrication of Transparent Electro-Optic Films for Optical Modulator," *Proceedings of the IMAPS/ACerS International conference and Exhibition on Ceramic Interconnect and Ceramic Microsystems Technologies,* April 24-27, 2006, Denver, CO.

11 J.H. Park *et al*., "Fabrication of Barium Strontium Titanate Films Directly on Copper Electrodes by Aerosol Deposition Method for Multilayer Dielectric Devices," *Proceedings of the IMAPS/ACerS International conference and Exhibition on Ceramic Interconnect and Ceramic Microsystems Technologies*, April 24-27, 2006, Denver, CO.

12 Y.J. Yoon *et al*., "Growth of BaTiO3-Ag Hybrid Composite Films at Room Temperature by Aerosol Deposition," *Trans. Nonferrous Me. Soc. China* **22** (2012) s735-739.

13 S. Baba and J. Akedo, "Fiber Laser Annealing of Nanocyrstalline PZT Thick Film Prepared by Aerosol Deposition," *Applied Surface Science* **255** (2009) 9791-9795.

5.2. Aerosol Deposition Process Parameters

In AD, deposition efficiency is extremely low as the majority of the particles impacting the target did not “stick” or contribute to coating buildup. The competition between deposition and erosion is always in play. Thus, process parameters must be chosen carefully and adjusted to increase deposition rate and minimize erosion rate.

The major process parameters in AD that affect particle velocity include particle size, carrier gas type, and aerosol generation chamber / spray deposition chamber pressure differential (38). A critical particle velocity for deposition was reported in (4) and was material-dependent. Other process parameters in AD that affect deposition efficiency include particle treatment, substrate material, and deposition angle. These process parameters must be optimized for different materials on different substrates. In addition, these process parameters must be optimized and post processing treatments must be performed to achieve different functional materials properties.

5.2.1. Particle Size and Treatment

As previously discussed in Section 3, particle size strongly affects deformation behavior and thus greatly influences the AD process outcome—consolidation vs. erosion. Submicron particles capable of deformation must be used in AD process to achieve consolidation. Particle treatment is reported to strongly influence deposition efficiency in the AD process. Many published studies have shown that vigorous ball-milling, powder annealing, and/or calcination significantly increase deposition efficiency (38). In most cases, parameters for particle treatment were identified empirically. For example, Akedo and Lebedev found that ball milling PZT particles for 5 hours increased their deposition rate by 30 times to 73 µm/min over a 5 mm^2 area (39). However, ball milling for an additional 30 hours reduced their deposition rate to ~30 µm/min. They also found that ball milling for 5 hours and subsequently heat treating PZT particles at 800°C for 4 hours in air resulted in a deposition rate of ~25 µm/min. It appeared that ball milling facilitated both particle deformation and particle-particle bonding in the AD process (38). Akedo and Lebedev assumed that ball milling changes particle surface properties—surface activation, defects, and gas absorption. In Section 4, we observed, through *in situ* TEM and molecular dynamics simulation, that dislocation nucleation and glide occurs during alumina particle deformation in compression. We hypothesized that ball milling would introduce mobile dislocations into the particle interior, thus facilitating particle plastic deformation during impact (28). Less energy is required to move existing mobile dislocations compared to nucleating new dislocations and then moving them. This means ball milled particles that contain mobile dislocations will deform more easily and will likely deform at lower particle velocity during impact. Annealing ball milled particles will cause polygonization—dislocation alignment to form subgrains—which was shown to increase deposition efficiency in the AD coating process (40). Importantly, excessive annealing will cause defect combination and dislocation annihilation, potentially lowering particle deformability; resulting in lower deposition rates (28). Moreover, based on atomistic simulation results published by Imakana *et al*. discussed earlier, ball milling creates many small particle fragments that become amorphized as they impact the substrate. This also facilitates particle-particle bonding responsible for coating consolidation (28).

In this LDRD, we will prove that submicron ceramic particles can create consolidated AD coatings and that micron sized ceramic particles result in substrate erosion. This will be discussed in Section 6, where we report single particle deposition experiments accomplished by accelerating a low concentration of 0.3µm and 3.0µm Al_2O_3 particles towards identical substrates. The influence of particle treatment on the AD process was beyond the scope of this LDRD and was not explored.

5.2.2. Carrier Gas

Particle carrier gas type has been shown to influence particle velocity, resulting in different residual stress and properties in AD ceramic coatings; however, the fundamental mechanisms responsible for these effects are not well understood (38). At identical flow rates, carrier gas type influences particle velocity, particle impact behavior, consolidation, and subsequent coating properties. At a gas flow rate of ~15 l/min, both alumina and PZT particle velocities were reported as 350 m/s in air and 500 m/s in He. Note that the critical velocity to achieve alumina deposition over erosion was reported to be ~150 m/s (6). The increased particle velocity in helium compared to air can be explained by helium’s small molecular size and consequent higher sonic velocity at any given flow rate.

Particle carrier gas type is also reported to influence coating residual stress and properties. Schubert *et al*. showed that use of an oxygen carrier gas produced a slightly oxygen enriched environment and created stoichiometric, white Al_2O_3 coatings, whereas, use of a nitrogen or helium rich carrier gas produced a reducing environment and created a non-stoichiometric gray $Al_2O_{3-\delta}$ coatings with oxygen vacancies (41). An interesting example of carrier gas and gas flow effects on AD coating optical properties was shown by Akedo (4). PZT particles suspended in helium carrier gas underwent plasma discharging during impact. This processing approach resulted in a dark gray PZT coating. It is thought that plasma discharging introduced defects into the consolidated PZT coating which in turn decreased the coating transmittance (4). In comparison, PZT particles suspended in nitrogen gas exhibited no plasma discharging during impact. This processing approach resulted in a yellow, transparent PZT coating (4).

Stoichiometry, crystallography, grain size, defect concentration, and residual stress in AD coatings can also be altered using post deposition annealing (38).

In this LDRD, we focus on the effects of particle carrier gas type—air vs. He—on particle velocity, particle splatting behavior upon impact, and consolidated coating microstructure (Section 6). The influence of particle carrier gas type on coating properties was beyond the scope of this LDRD and was not explored.

5.2.3. Substrate Type (Relative Hardness)

The relative strength and hardness between the coating material and the substrate must be considered when selecting AD process parameters. If the substrate's hardness is similar to or greater than that of the depositing material, the substrate will support the particle deformation and allow anchoring layer to adhere as the impact energy is converted to bonding energy. For example, a sapphire or zirconia substrate would be able to sustain the impact of high velocity submicron alumina particles. This allows an initial buildup of an anchoring layer of deformed/adhered particles, consequently allowing subsequent particles to build upon themselves for coating consolidation.

Alternatively, if the substrate's hardness is lower than that of the depositing material, the substrate will not support particle deformation and the process parameters must be modified to provide lower particle velocity. The initial buildup of an anchoring layer will only be possible by particle embedding during impact. For example, a copper substrate cannot support the impact of high velocity submicron alumina particles and will erode. However, low velocity submicron alumina particles may be able to embed themselves in the copper substrate, forming an initial anchoring layer, thus allowing subsequent particles to build upon themselves and form a coating.

In this LDRD, we focus on deposition of submicron alumina particles on substrates with equal relative hardness such as sapphire and those with lower relative hardness such as silicon.

5.2.4. Impact Angle

As reported by Akedo (4), deposition is optimal when the particle stream is perpendicular to the substrate surface. Any deviation from perpendicular will increase erosion. As the impact angle deviates from perpendicular, erosion eventually overtakes deposition.

All experiments conducted in this LDRD used a particle stream that was oriented perpendicular to the substrate surface. The effect of impact angle on deposition behavior was beyond the scope of this LDRD and was not explored.

5.2.5. Stage Traverse Speed

Achieving relative movement between the particle stream and the substrate appeared important but was not explicitly discussed in literature. The apparent benefit of traversing the particle stream across the substrate was agility in patterning the coating. However, the effect of traverse speed on coating deposition was not discussed.

We speculated that traversing the particle stream over the substrate increases the amount of deposited materials interacting with the substrates, thus increasing the numbers of particles that contribute to deposition. Most of the experiments in this LDRD used a traverse speed of 20 mm/s. The effect of traverse speed on deposition was beyond the scope of this LDRD and was not explored.

5.2.6. Post Process Annealing Treatment

The as-deposited coatings are reported to have very small grain size (20−75 nm or less). Small grain size may be beneficial for structural ceramics, but larger grain sizes are often desirable to maximize other properties (38). Post deposition annealing treatment can be performed to achieve grain growth for stress relaxation and/or improve optical, electrical, magnetic, and piezoelectric properties (38).

Schubert *et al*. produced 9 µm AD Al_2O_3 coatings on Al_2O_3 substrates using nitrogen carrier gas, heat treated them, and examined coating residual stress (40). The as deposited coatings showed highly compressive residual stress at 2.1 GPa. Coating residual stress decreased with increased annealing temperature and completely relaxed at temperatures above 300°C. Higher annealing temperatures have also been reported to achieve grain growth and alter coating properties. For example, Inoue *et al*. (42) showed annealing $Bi_{0.5}Y_{2.5}Fe_5O_{12}$ (Bi:YIG) AD coatings in air at 800°C for 10 minutes, increased the grain size from 15 nm to 28 nm and increased the saturation magnetization ($4\pi M_s$) from 0.25 kG to 1.1 kG. Another example by Furuta *et al*. (43) showed a dense $BaTiO_3$ thick film fabricated by the AD method was crystallized and detached from the substrate using an annealing treatment at 600°C. Subsequently, annealing was performed at various temperatures, resulting in freestanding $BaTiO_3$ thick films with grain sizes from 24 nm to 170 nm. Polarization-electric field (P-E) measurement revealed that $BaTiO_3$ ceramics with grain sizes of more than 58 nm showed ferroelectricity, whereas $BaTiO_3$ ceramics with an average grain size of 24 nm showed paraelectricity at RT. Dielectric measurement indicated that the permittivity decreased with decreasing grain size in the range of 170 nm to 24 nm.

In this LDRD, we did not perform statistical analysis of the as-deposited film grain size; nor did we explore post process annealing treatment. Future work should explore ex-situ annealing treatment as well as in-process annealing treatment to achieve grain growth in the AD layers while minimizing heat transfer to the underlying structures/parts.

6. AEROSOL DEPOSITION

The work in this section was done in collaboration with Ronald C. Dykhuizen, Joshua A. Hubbard, Steven Storch, Michael P. Saavedra, James F. McCloskey, Amy Allen, Bonnie B. McKenzie, Joseph a. Padilla, Harlan Brown-Shaklee, Adam W. Cook, and David M. Keicher.

6.1. SNL’s Aerosol Deposition System

An aerosol deposition system was constructed at SNL’s Thermal Spray Research Laboratory (TSRL) and is shown in Figure 14. A carrier gas source (compressed air and/or compressed helium) was supplied to a commercial rotating brush generator (RBG) that was used for aerosol generation and delivery. The aerosol generation chamber was capable of operation between 3–26 psi (52–1345 torr). Conductive tubing approved for use in vacuum was used to connect the aerosol generator to the nozzle in the vacuum chamber. The TSRL’s Controlled Atmosphere Plasma Spray chamber, was used as the deposition chamber. The deposition chamber has an operational range of 0.2–630 torr (note that Albuquerque’s atmospheric pressure is 630 torr). A commercial X-Y stage was integrated into the chamber for moving the substrate. The stage is capable of movement at a speed as high as 25 mm/s.

As mentioned above, the deposition nozzle design was modified from that reported by Chun *et al*. (13). The converging/diverging geometry of the nozzle increases the carrier gas and particle velocities. Calculated particle velocity will be discussed in the next section. The nozzle throat cross-sectional area is 1 mm^2 and spans a 1 mm length. Then the nozzle diverges linearly, spans a 5 mm length from the throat to the nozzle exit. The nozzle exit cross-sectional area is 3 mm^2.

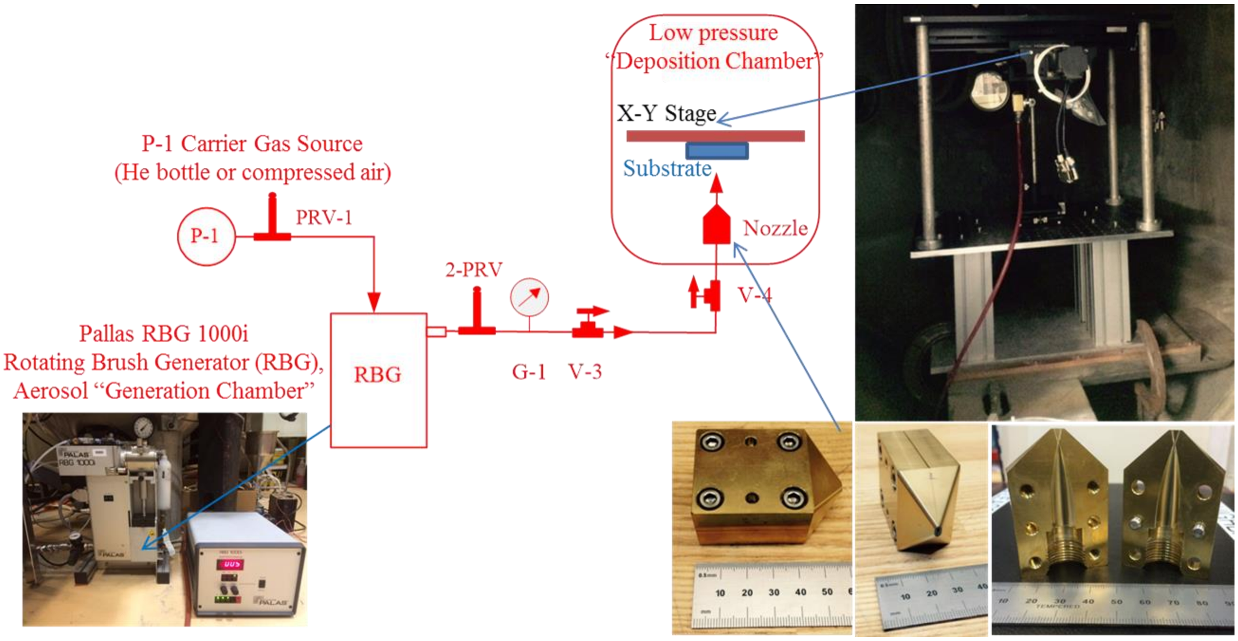

Figure 14: SNL’s Aerosol Deposition System constructed at TSRL.

6.2. Calculated Particle Velocity

An existing particle laden flow model originally developed for calculating a 1-D particle velocity in cold and plasma spray processes by Dykhuizen *et al*. was used to estimate AD particle velocities (44-46). The code predicts gas and particle velocities as they enter and exit the nozzle. The code takes into account nozzle geometry, gas type, inlet gas pressure, exit pressure, particle size, and particle properties (density, heat capacity, etc.). Thus, we believe the code is adequate for calculating particle velocity in the Aerosol Deposition process. Note that once the particles exit the nozzle, the code is no longer applicable in capturing the particle interaction with the vacuum environment and is not capable of predicting particle velocity during impact. A more sophisticated modeling tool such as CFD would be needed to predict particle velocity at impact. We use this code as a tool to understand the effect of particle size, nozzle geometry, and carrier gas type/pressure on the maximum achievable particle velocity at different deposition conditions.

Using nozzle design and process conditions given by Chun *et al*. (13) as input to the code, the particle velocity inside the nozzle was calculated. A comparison of particle velocity in the nozzle calculated using the SNL 1-D code and provided by CFD modeling from Chun *et al*. is shown in Figure 15. The calculated particle velocity at the nozzle exit is 562 m/s using SNL's code and is ~550 m/s using Chun et al.'s data (estimated from graph). While the predicted particle velocity at nozzle exits may not be exactly the same, we believe the SNL code is sufficiently accurate for estimating particle velocity. Thus, the SNL 1-D particle velocity code by Dykhuizen *et. al*. was used to inform deposition parameter selection and design experiments in this LDRD.

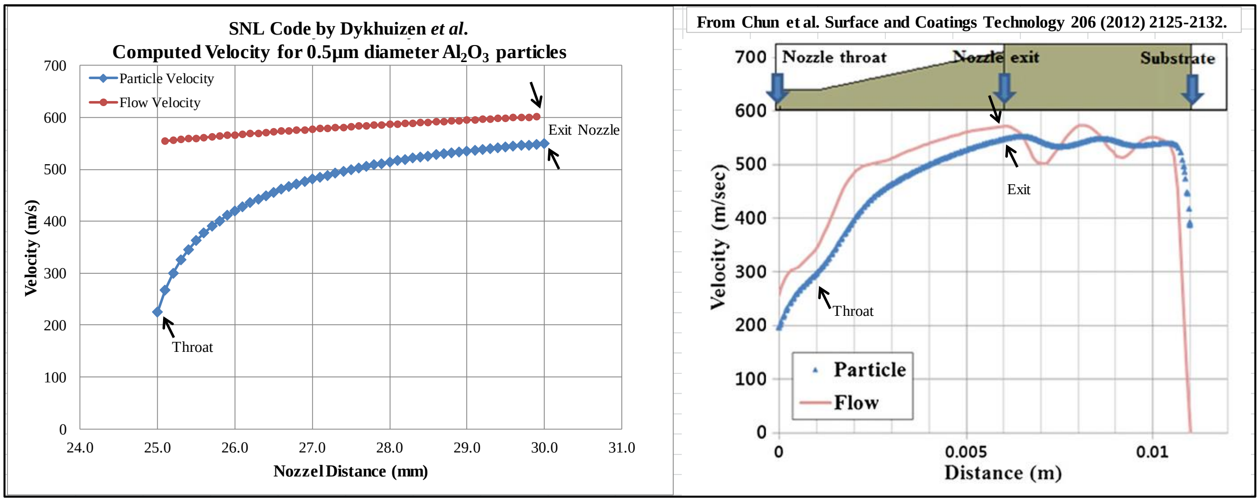

Figure 15: Calculated gas and particle velocity along the nozzle using parameters given by Chun et al. (13). Left, SNL's Dykhuizen *et al*.'s code and Right, from figure 7 in (13).

Next, the SNL code was used to investigate calculated particle velocity as a function of carrier gas type, aerosol generation chamber pressure and deposition chamber pressure. The SNL code predicted that choked flow is achieved for all gasses when pressure in the aerosol generation chamber exceeds 5psi. It also predicted that once critical flow is achieved the particle velocity in the nozzle is unaffected by the deposition chamber pressure (similar particle velocities were predicted at all pressures below 300 torr). Thus, for a given nozzle geometry, particle size/material, the particle velocity (within our system and existing equipment capability) is only a function of aerosol generation chamber pressure and carrier gas type. Particle velocities at the nozzle exit for 3.0µm and 0.3µm Al_2O_3 particles are shown in Figure 16 and Figure 17, respectively. Note that the literature value of critical velocity for aerosol deposition using submicron Al_2O_3 particles was reported to be 150 m/s (6). It appeared that our current nozzle geometry restricted us to particle velocity of >190 m/s for the 3.0µm particles and >400 m/s for the 0.3µm particles. This allowed proof of concept demonstration for particle deposition but may not allow full optimization of the deposition process. We recommend engineering different nozzle geometries capable of reaching lower velocities for future work.

The relative particle velocity is shown in Figure 18. It appeared that the velocity of a 0.3µm particle can be 87%-262% faster than the velocity of a 3.0µm particle, depending on the carrier gas type and generation chamber pressure. In this LDRD, we only used one nozzle geometry and we selected air and helium as the particle carrier gases so that both the lower and higher velocity ranges could be explored. Future work should explore changing nozzle geometry to reach a lower range of particle velocities.

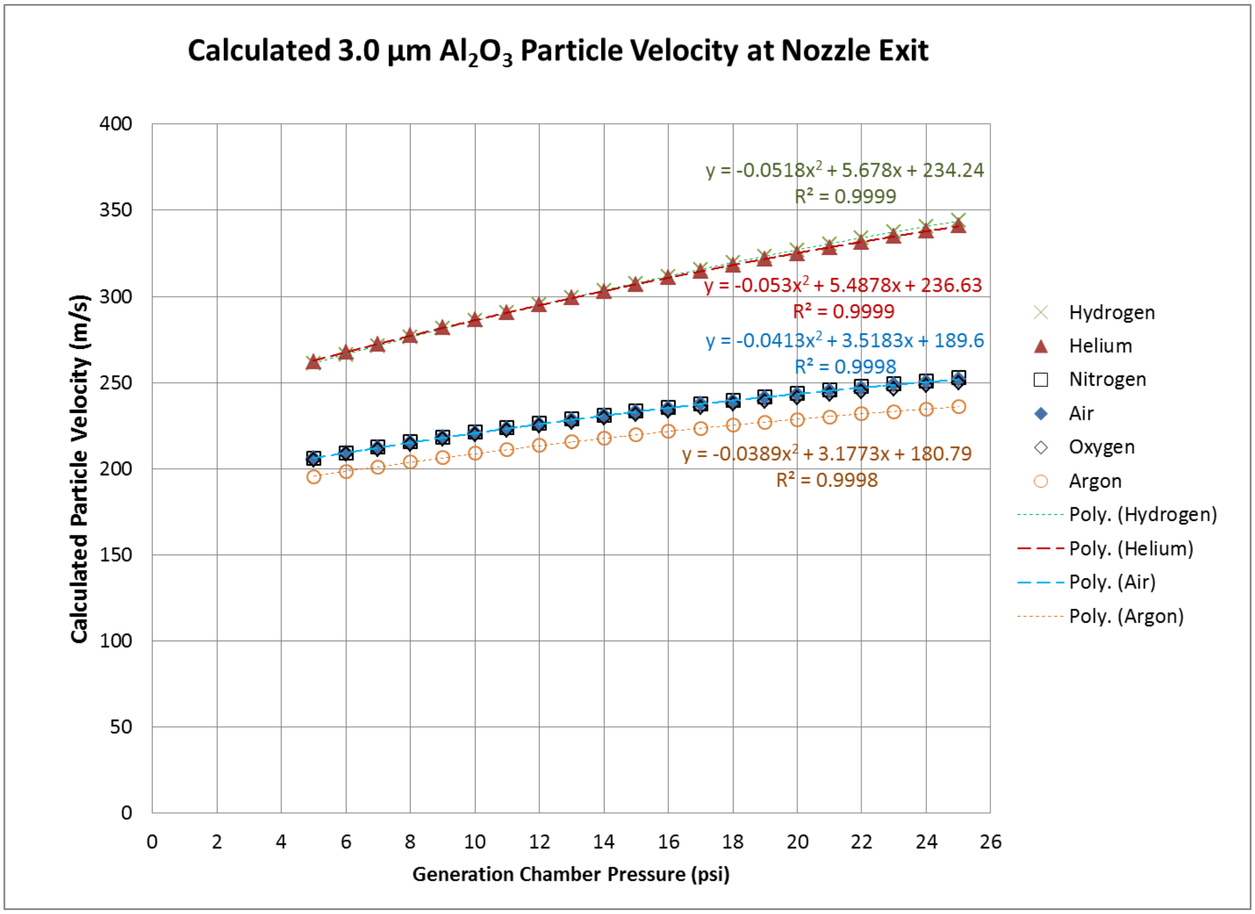

Figure 16: Calculated 3.0µm Al_2O_3 particle velocities at the nozzle exit as a function of carrier gas type and generation chamber pressure.

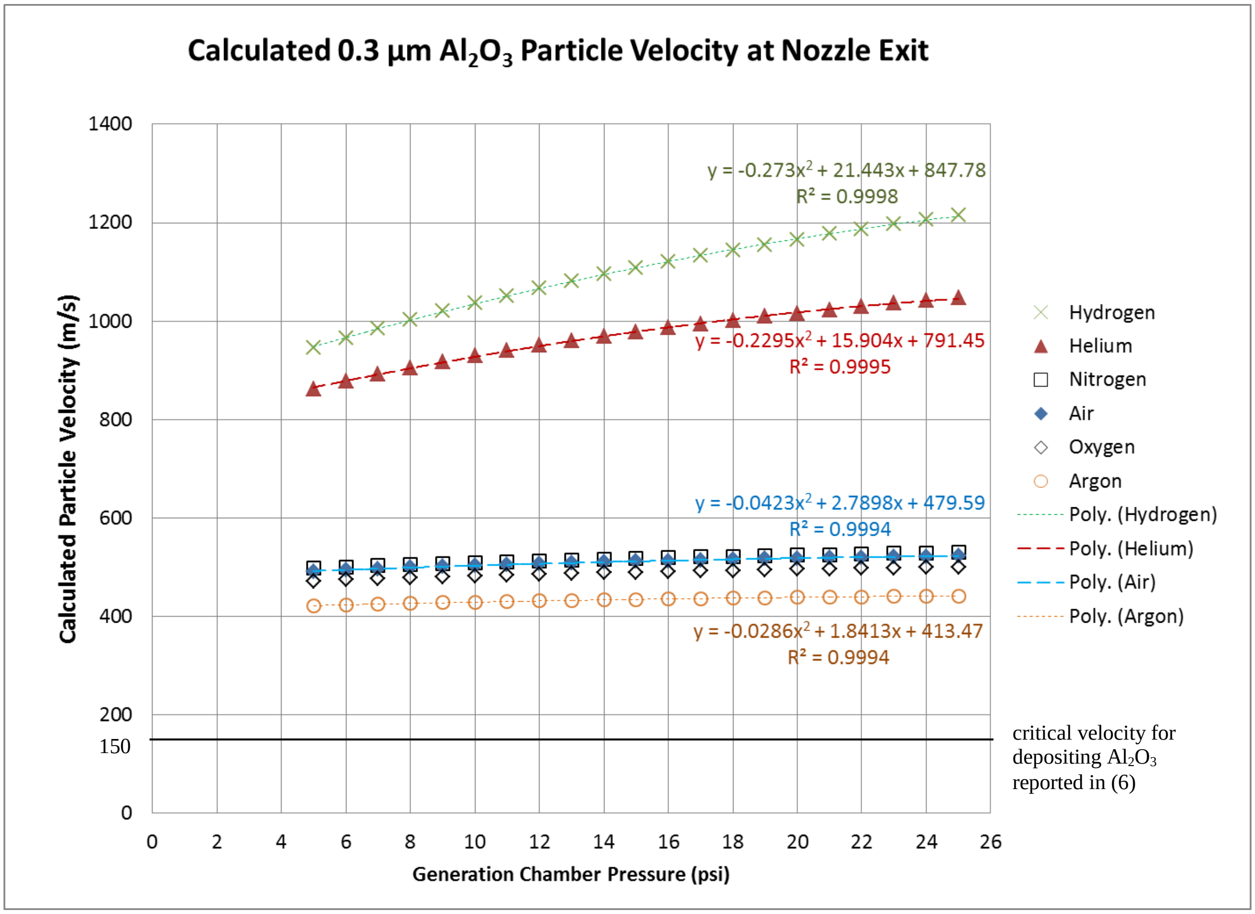

Figure 17: Calculated 0.3µm Al_2O_3 particle velocities at the nozzle exit as a function of carrier gas type and generation chamber pressure.

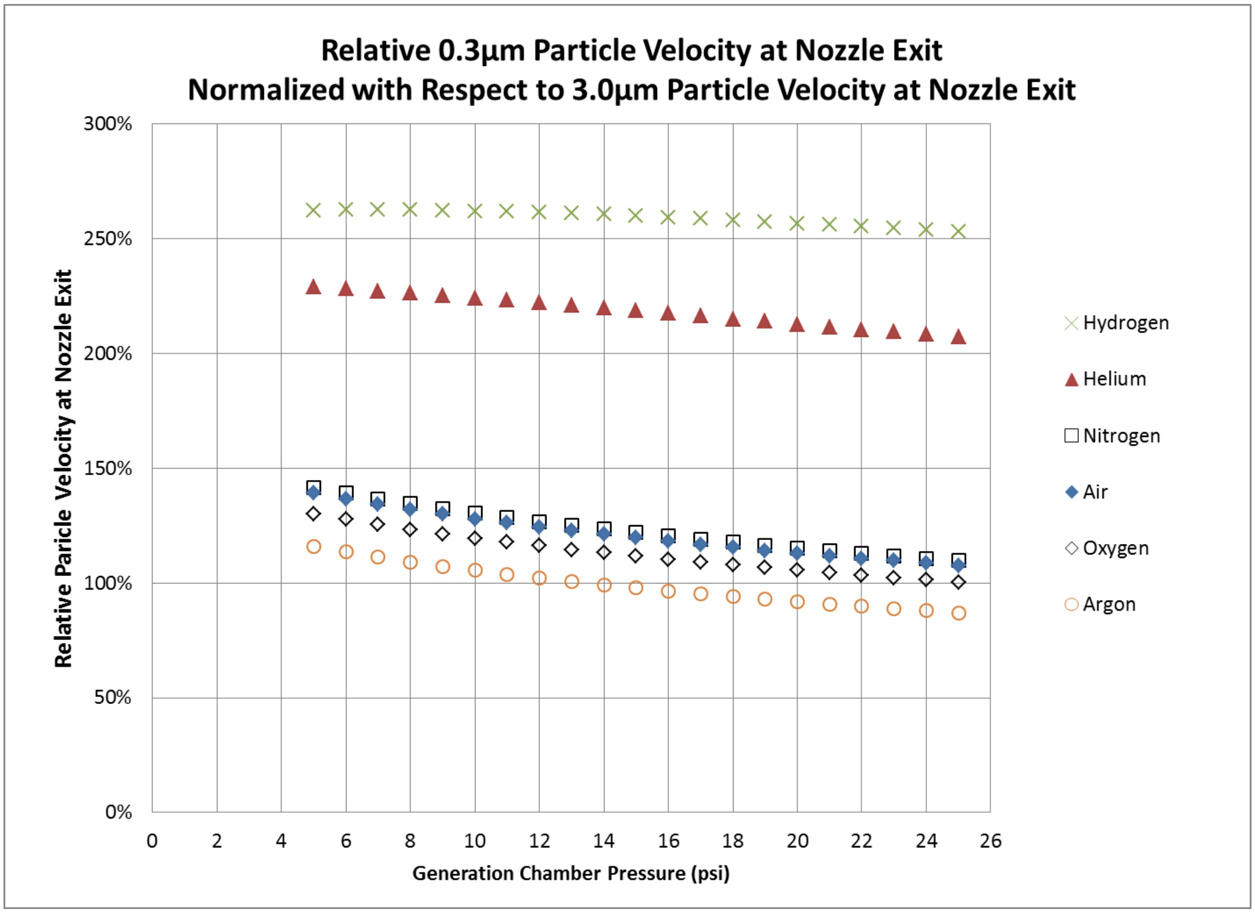

Figure 18: Relative 0.3µm Al_2O_3 particle velocities at the nozzle exit normalized with respect to 3.0µm particle velocities at the nozzle exit as a function of generation chamber pressure and carrier gas type.

6.3. Simulated Particle Impact on Substrate

We have performed simulations of the aerosol deposition process by accelerating ceramic particles at high velocity until they impact on a substrate. The same particles described in the simulations in Section 4.3 were used, namely single crystal Al_2O_3 particles with a 5 nm radius, oriented with the 0001 plane in the impact direction (z). The substrate was also a single crystal Al_2O_3 with the same orientation. Particles were initially placed with a 2 nm separation between the bottom of the particle and the top of the substrate, and given an initial velocity of 400-1000 m/s in the negative z direction (see Figure 19a). The substrate was approximately a cube 20 nm on each side, with multiple regions defined as follows in order to describe impact. The bottom 1.2 nm of the substrate was held fixed. Above this region, was 13 nm of material that had a Langevin thermostat applied to maintain a temperature of 300K. Of this region, the lower 8.8 nm (directly above the rigid atoms) additionally had viscous damping applied in order to prevent finite size effects that can occur from dislocations travelling through the substrate and reflecting at the boundary. These simulations were performed with both the force field from Garofalini, described above, as well as with a ReaxFF reactive force field developed by Pittman and van Duin (47) for simulations of clay-zeolite composites that can accurately treat the relevant species in this system.

We found in all cases studied to date, regardless of particle velocity or amount of viscous damping, that particles impacting single crystal substrates are reflected from the substrate without serious deformation. As shown in Figure 19b, the initial impact causes elastic deformation of the substrate that leads to slowing of the particle, and eventual reversal as the particle is accelerated in the positive z direction. Depending on initial velocity, there can be material from the particle that is left on the substrate Figure 19c, but in no cases do we find plastic deformation or adhesion, as in the experiments. Previous simulations by other groups (15) have indicated that this phenomenon is due to the choice of substrate, and that even a thin layer of amorphous material on the substrate (or an initially amorphous substrate), would significantly alter the impact behavior of the particle. These simulations are currently underway in order to more accurately reflect the experimental procedure.

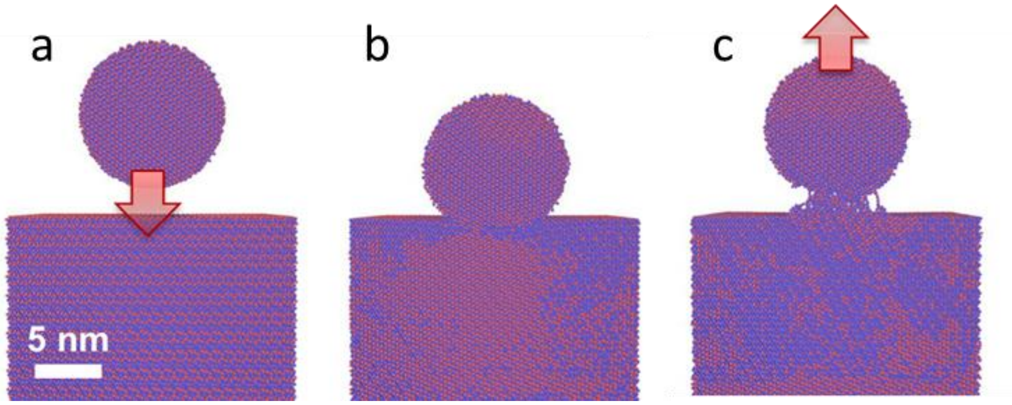

Figure 19: Thin slices through a 10 nm NP and the sapphire substrate, showing atom positions at different stages of deposition. The NP has the {0001} plane perpendicular to the impact direction and the sapphire substrate also has the {0001} plane oriented perpendicular to the impact direction. (a) Moment before impact; (b) during impact; (c) NP rebounded off from the sapphire substrate surface, leaving behind residue.

6.4. Single Particle Deposition Experiments

The objective of this section is to understand how the individual micron (3.0µm) and submicron (0.3µm) sized alumina particles behave after they undergo high strain-rate deformation as a result of their impact, at varying velocities, on the sapphire substrate. The aerosol chamber pressure was set at 20 psig and the deposition chamber was set at 5.8 psi (300 torr). Both the 3.0µm and the 0.3 µm particles were suspended in air and accelerated towards the substrate simultaneously. The traverse speed was varied for three different spray runs at 0.5, 10, and 20 mm/s. The calculated particle velocity is shown in Figure 20, with the exit velocities of 243 m/s and 518 m/s for the 3.0µm and the 0.3µm particles, respectively. It is expected that the particle velocity will drop substantially as the particles traverse the 5mm space between the nozzle exit and the sapphire substrate.

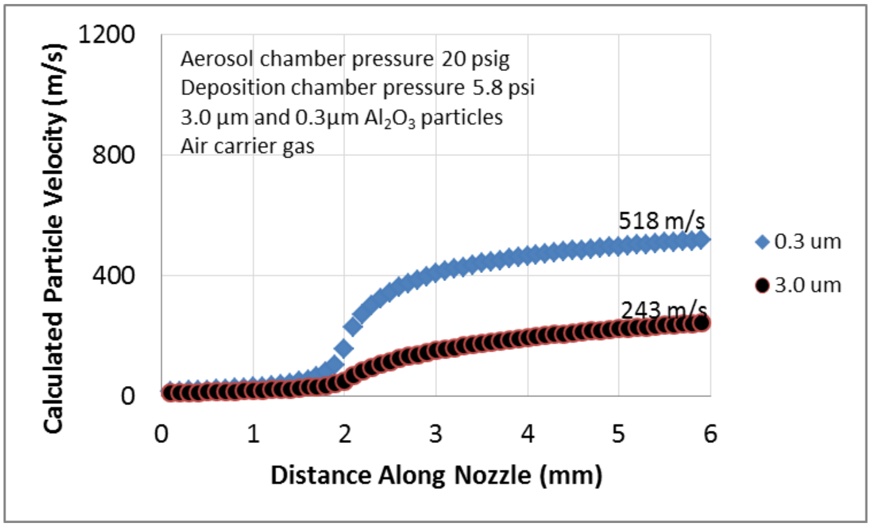

Figure 20: Calculated velocity (with air as carrier gas) for the 3.0µm and 0.3µm Al_2O_3 particles.

The sapphire substrate was examined in the SEM after deposition. SEM images comparing the blank sapphire substrate (away from the deposition region) and the substrate in the deposition region are displayed in Figure 21. Many large craters, up to 1µm in length, were found on the substrate (marked by solid circles in Figure 21). These craters were created by the 3.0µm particles impacting and damaging the substrate. Single particle "splats" were also observed (marked by arrows in Figure 21). These were created by the 0.3µm particles impacting, deforming, and changing into pancake shaped grains that adhere to the sapphire substrates. The splatted particles appear strikingly similar to one of the 0.3µm particles that were compressed at an extreme loading condition using the Hysitron PI85 SEM Picoindenter from Section 3. The comparison is shown in Figure 22.

TEM samples from the splatted alumina particles on the sapphire substrate were prepared using the FIB lift out technique. The samples were examined in the TEM to understand particle deformation and bonding to the substrate. In general, TEM examination revealed the undisturbed substrate was free of defects and dislocations whereas the substrate area that was hit by a particle was deformed. An example is shown in Figure 23. Figure 23A shows dislocations under the surface crater (made by particle impacting and bouncing off) in the substrate. Figures 23A-D show a splatted Al_2O_3 particle and the underlying deformed substrate. Examining closely at the particle/substrate interface, we observed regions with bonding towards the middle of the particle and regions containing gaps towards the outer edge of the particle. The higher magnification TEM image of the bonded area showed a very small disordered layer at the particle/substrate interface. It appeared that the kinetic energy in the traveling particles facilitated the deformation and mechanical bonding of the particle and the substrate. In addition, it is probable that there is chemical bonding between the particles and the substrate. Moreover, the splatted particles contain 15-30 nm nanocrystallites, indicating that the splatted particles not only deformed but fractured into many different subgrains without fragmentation. Diffraction patterns collected from another splatted particle revealed that the splat is polycrystalline with mosaicity as shown in Figure 24. Submicron particle deformation, shape change, and polycrystallinity with mosaicity were demonstrated in both the quasi-static, low strain rate loading using the micro-compression experiments discussed in Section 4 as well as in the dynamic, high strain rate loading from impact in the single particle deposition experiments described here. Thus, it is concluded that submicron particle size is needed for successful consolidation of AD coatings.

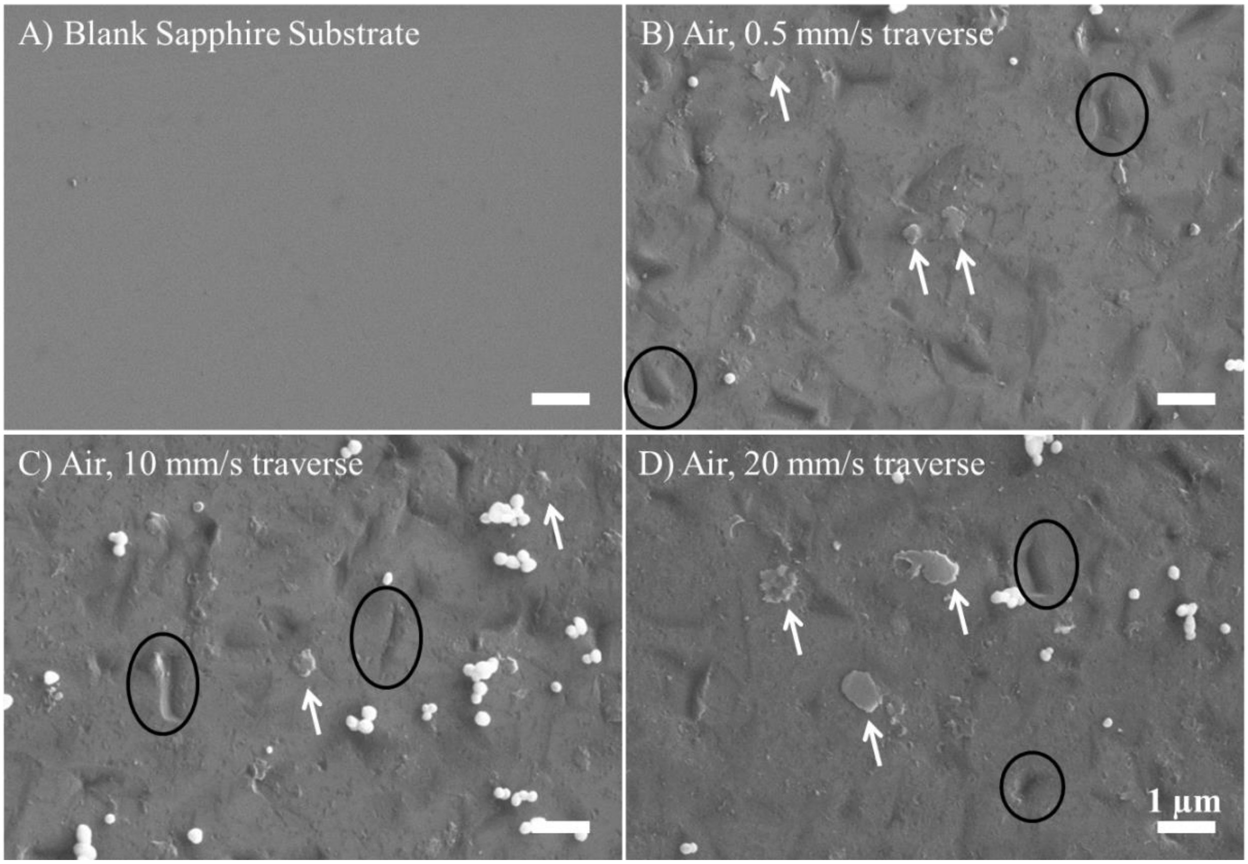

Figure 21: SEM images of the blank sapphire substrate, away from the deposition region (A), and sapphire substrates in the deposition region for runs with both 3.0µm and 0.3µm Al_2O_3 particles at traverse speeds of 0.5 mm/s (B), 10 mm/s (C), and 20 mm/s (D). The circles in the images identified craters from the impact of 3.0µm Al_2O_3 particles and the arrows in the images identified splats from the deformed 0.3µm Al_2O_3 particles.

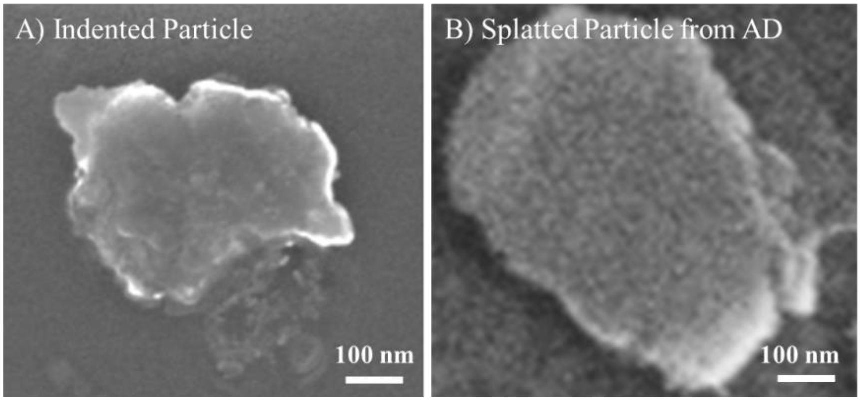

Figure 22: SEM images of the submicron Al_2O_3 particles (A) indented using the Hysitron PI85 SEM Picoindenter at extreme loading and (B) splatted particles from the aerosol deposition process.

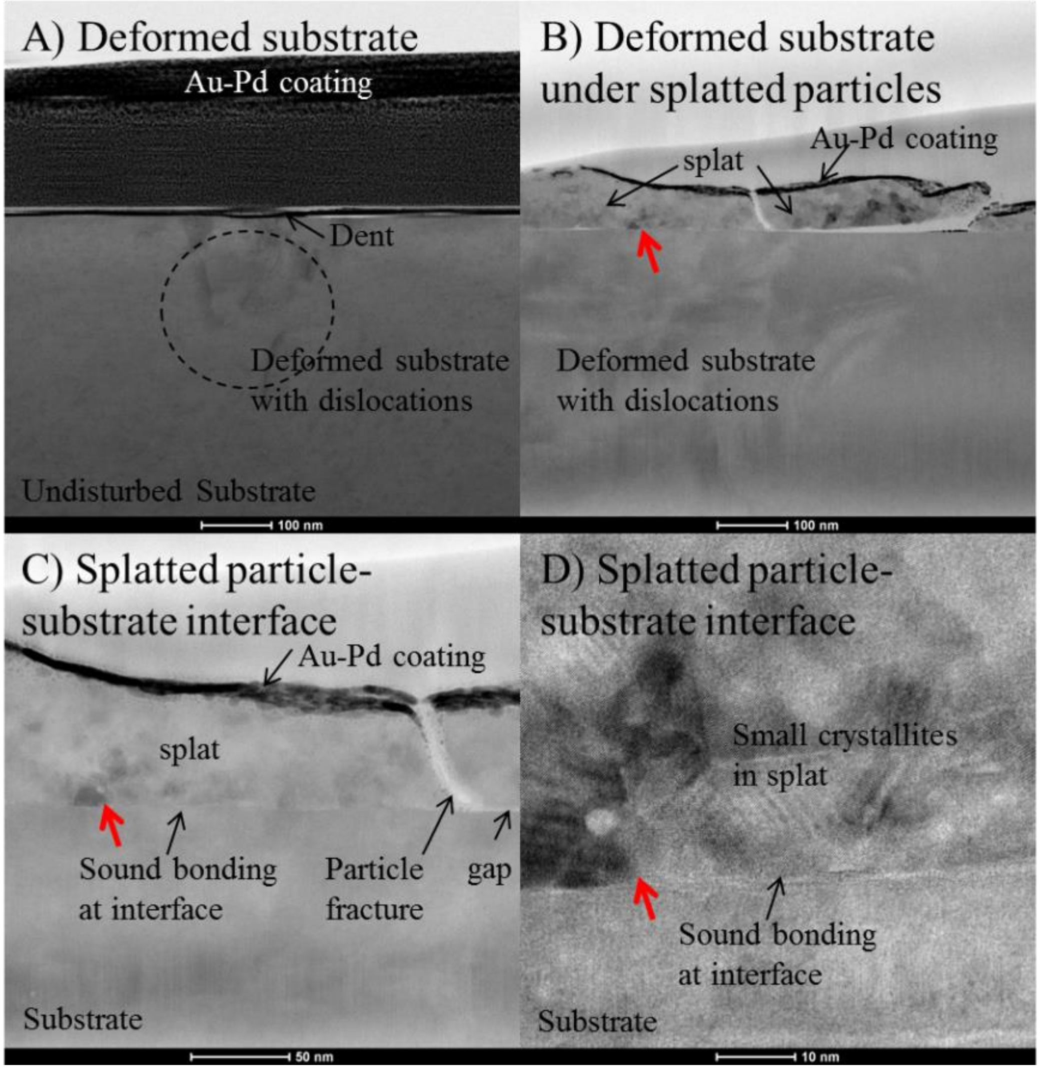

Figure 23: Bright field TEM showing (A) the deformed substrate from particle impact where the particle did not stick, (B) the deformed substrate under a splatted particle, (C) the splatted particle-substrate interface at low magnification, and (D) the splatted particle-substrate interface at high magnification.

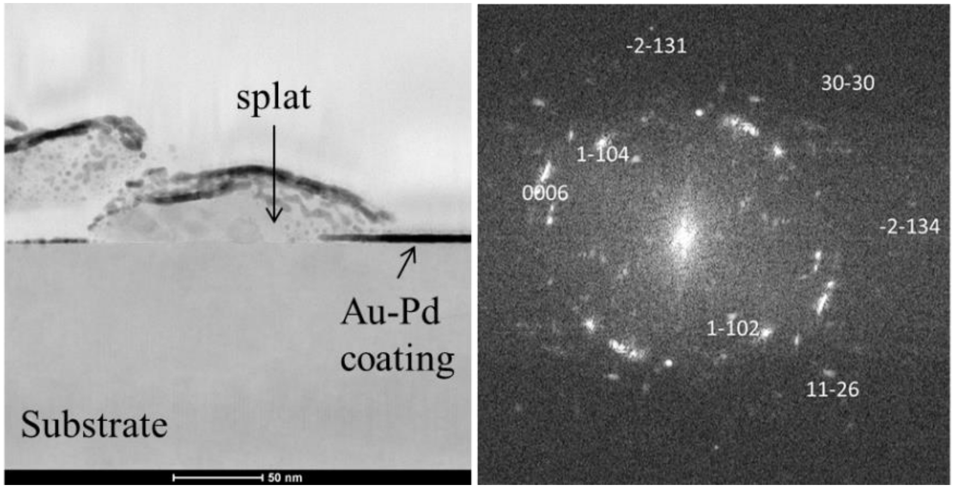

Figure 24: Bright field TEM image of a second splatted Al_2O_3 particle on the sapphire substrate and the Fourier transform of the entire splat showing polycrystallinity and mosaicity.

6.5. Consolidated Film Deposition Experiments

Thus far, we have demonstrated that submicron ceramic particles can plastically deform in compression using indentation experiments (Section 4.4) as well as single particle deposition experiments (Section 6.4). Moreover, we have also demonstrated that 3.0µm particles resulted in erosion whereas 0.3µm particles resulted in splat formation and adhesion to the substrate. In this section, the quantity of 0.3µm particles was increased to generate more splats and create consolidated films.

First, the parameters used in the single particle deposition experiment described in Section 6.4 were repeated. Air was used as the carrier gas, the aerosol chamber pressure was set at 20 psig, and the deposition chamber was set at 5.8 psi (300 torr). The traverse speed was 20 mm/s and the standoff distance was 5 mm. We attempted to deposit Al_2O_3 on sapphire but did not get a consolidated film. The SNL code was used to estimate particle velocity at the nozzle exit. It was found that using helium as a carrier gas will double the particle velocity, as shown in Figure 25. Subsequently, helium was used as the carrier gas with the aerosol chamber pressure of 5 psig and 20 psig. In both cases, we were able to deposit continuous Al_2O_3 films on sapphire substrates.

Next, Al_2O_3 was deposited on sapphire substrates, using helium as carrier gas with the aerosol chamber pressure of 25 psig and the deposition chamber of 0.05 psi (2.4 torr). This should provide particle velocities at the nozzle exit of ~1050 m/s (Figure 17). A traverse speed of 20 mm/s (back and forth to make a stripe of coating), a standoff distance of 5 mm, and a run time of 15 minutes were used. The sample image and the SEM image of the film top surface are shown in Figure 26. Subsequently, TEM liftouts from the film/substrate were prepared using the FIB. The samples were examined in the TEM to understand particle-substrate bonding and particle-particle bonding.

In general, TEM examination revealed the undisturbed substrate was free of defects and dislocations whereas the substrate area beneath the coating was highly deformed and the substrate surface was dented. Dislocations were found at distances up to 1.5 µm away from coating/substrate interface. An example is shown in Figure 27. Figure 27A clearly shows a coating/substrate interface that is rough and non-uniform. The coating is also non-uniform with a nominal thickness of ~50 nm. Figure 27B-C shows the aerosol deposited nanocrystalline Al_2O_3 coating and the underlying deformed/dented alumina substrate with characteristic dislocations. Examining more closely at higher magnification Figure 27D-F, we observed some regions of the film with measured thickness >100 nm. The film appeared to be almost 100% dense.

Complete bonding was observed between the particles and the substrate as well as between the particles within the film. It was extremely difficult to identify particle boundaries as the film appeared to be a dense polycrystalline structure, consisting of 15–30 nm crystallites. It appears that the particle kinetic energy facilitated not only the deformation and the particle-substrate bonding as shown in Section 6.4, but also the compaction or "tamping" of the previous layer of particles, providing complete particle-particle bonding. The tamping effect has been discussed in the literature (40, 48-50).

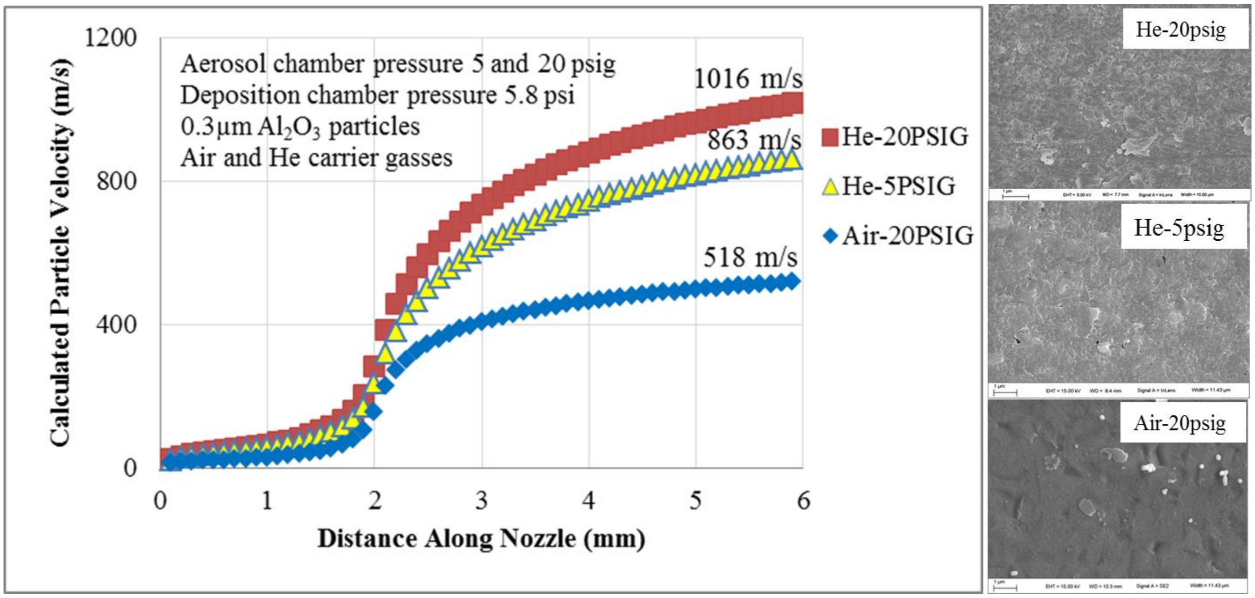

Figure 25: Calculated 0.3µm Al_2O_3 particle velocities at the nozzle exit using air and He as carrier gases for a fixed deposition chamber pressure of 5.8 psi and varying inlet pressures of 5 and 20 psig. SEM images of the corresponding coatings are shown on the right.

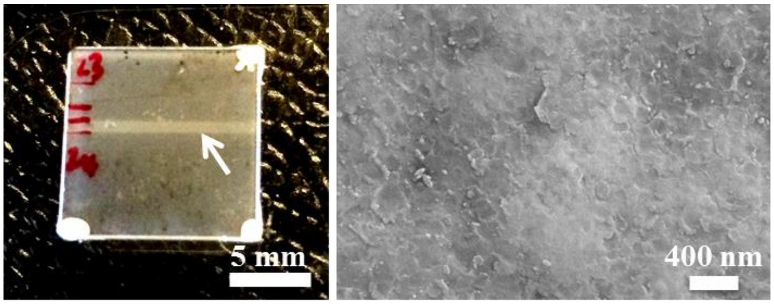

Figure 26: Top view of AD Al_2O_3 coating stripe on sapphire substrate (left) and an SEM image of the coating surface (right).

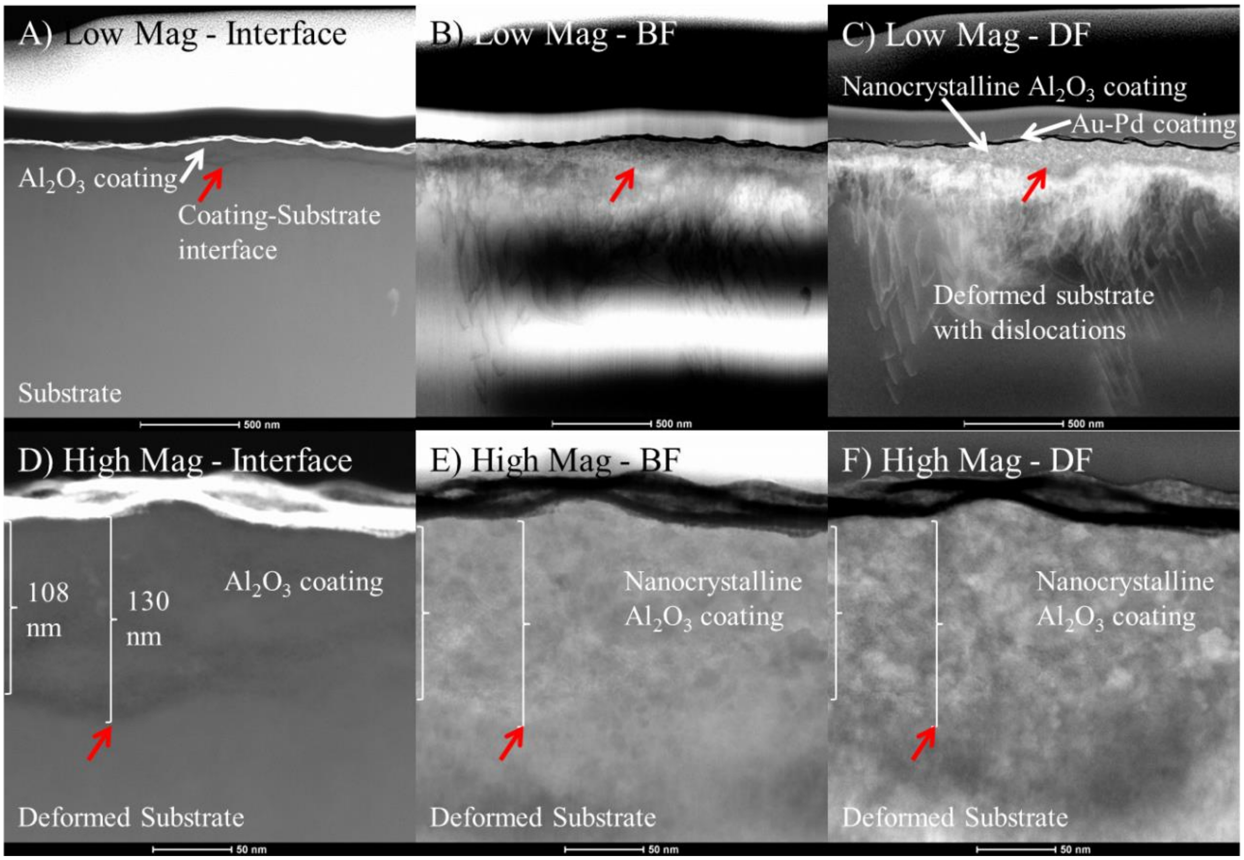

Figure 27: TEM images (Annular dark field (AD), Bright field (BF), and Dark Field (DF) showing a cross-section through the aerosol deposited Nanocrystalline Al_2O_3 coating on sapphire substrate at low (A-C) and high (D-F) magnifications.

From the above experiment and microstructural examination, it appears that the tamping effect highly influences the coating microstructure and buildup. In the next experiment, we altered particle velocity and thus the tamping effect by changing the carrier gas. We set the aerosol chamber pressure at 25 psig and the deposition chamber at 0.02–0.05 psi (1–2.5 torr). The traverse speed was 20 mm/s and the standoff distance was 5 mm. The carrier gasses were either 100%He or 50%He+50%air. We expected to have consolidated films from both conditions, with the 100%He run providing higher particle velocity and thus higher degree of tamping. The coating surfaces from each sample were examined in the SEM and are shown in Figure 28. It is clear that the coating surface from the 100%He run appeared smoother. The edges of the surface particles were flush with the coating surface. In comparison, the coating surface from the 50%He-50%air run appeared rough and individual splats can easily be distinguished from one another. The edges of the surface splats were raised, similar to those found in the single particle deposition experiment in Section 6.4, Figure 21B-D and Figure 22B. This is indicative of bonding towards the middle of the particle and the presence of gaps around the particle edges. Thus, it was concluded that higher particle velocities (from using 100%He) provide a higher degree of tamping and more complete bonding between the particles and the substrate as well as between the particles in the film.

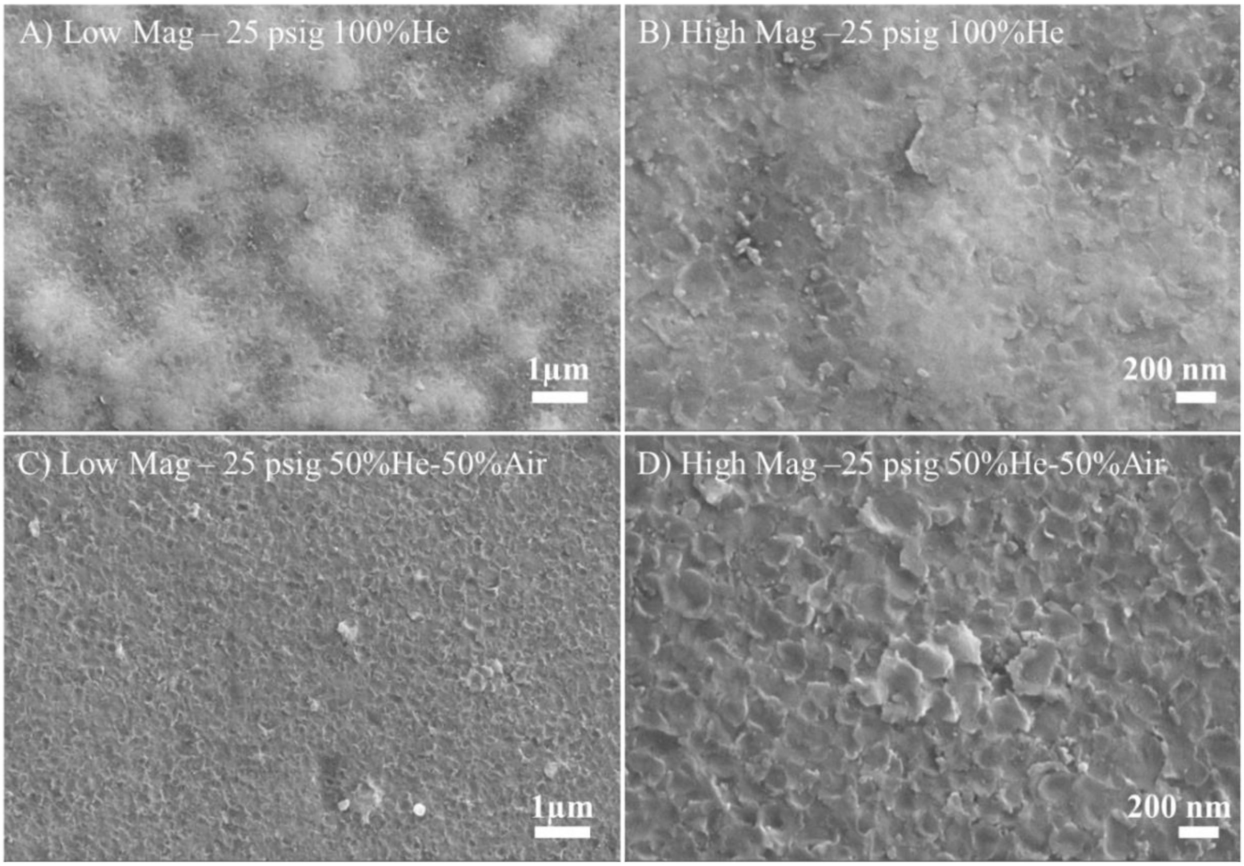

Figure 28: SEM images of the aerosol deposited Al_2O_3 coating surface. The aerosol chamber pressure was 25 psig; A) using 100% He and B) using 50% He and 50% air. The coating top surface has rough topography, creating low and high areas that appear as darker and lighter grey in the SEM images. Different carrier gases provided different particle velocities and changed the coating densification.

We have demonstrated aerosol deposition of Al_2O_3 on hard substrates such as sapphire. In the next experiment, we attempted to deposit on a relatively “soft” substrate (compared to Al_2O_3), such as a polished silicon wafer. We expected that lower particle velocity would be needed to avoid erosion and create a deposit on the softer substrate. Thus, we selected parameters that produced lower particle velocities using the current nozzle and setup. The 50%air+50%helium mixture was used as the carrier gas, the aerosol chamber pressure was adjusted to produce 3 psig at the nozzle entrance, and the deposition chamber pressure was set to 0.008 psi (420 mtorr). The particle velocity at nozzle exit was calculated to be 597 m/s. The traverse speed was 20 mm/s, the standoff distance was 5 mm, and the run was 2 hours long. The optical image of the sample surface and the SEM images of the coating surface are shown in Figure 29. Subsequently, the silicon was cleaved and the sample cross-section was examined in the SEM as shown in Figure 30. The average film thickness from 25 measurements was 147±19 nm. We speculated that the particle velocity was restricted by the nozzle geometry and was still too fast. We recommend changing the nozzle geometry in the future to reduce the particle velocity for deposition on softer substrates (note that the critical velocity to achieve alumina deposition instead of erosion was reported to be only ~150 m/s) (6)).

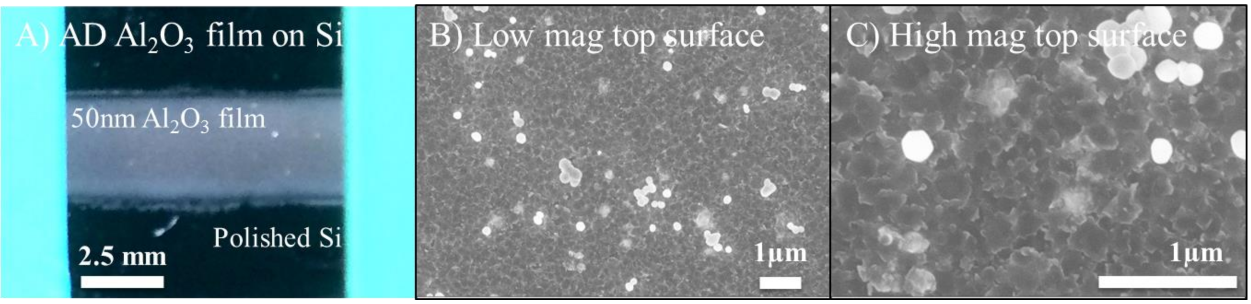

Figure 29: (A) Top view of an AD Al_2O_3 coating stripe on a polished silicon wafer (B) Low magnification and (C) high magnification SEM images of the top surface of the AD Al_2O_3 coating deposited on a polished silicon wafer. Splats are present as part of the consolidated film and loose particles can be seen on the film surface.

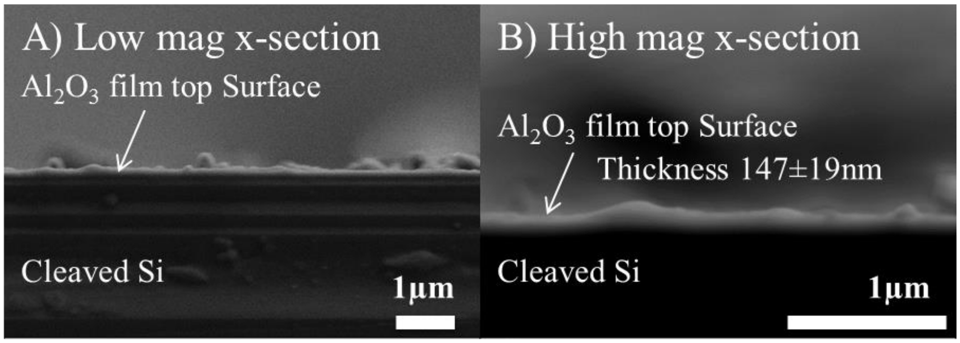

Figure 30: SEM images of the cleaved silicon wafer and AD Al_2O_3 coating. Coating thickness was measured in 25 locations and averaged to be 147 ± 19 nm.

We speculated that while the nature of particle-substrate and particle-particle bonding is mechanical, excellent adhesion is formed between particles in the consolidated film and between the anchoring particle layer and the substrate. We also speculated that the film likely contains high compressive residual stress from the particle impact and that the underlying substrate, sapphire or silicon in this case, likely accumulates more "damage" over time as the more tamping occurs and the film builds up (40, 48-50).

6.6. Proposed Bonding Mechanisms

Thus far, we have demonstrated that submicron ceramic particles can be plastically deformed in compression in indentation experiments (Section 4.4) as well as in single particle deposition experiments (Section 6.4). Moreover, we have also demonstrated that the submicron (0.3µm) particles are needed to achieve deformation and consolidation (Section 6.5). TEM observation of the Al_2O_3 particle-sapphire substrate interface revealed mechanical bonding underneath the middle of each splatted particle and some gaps around the edges. TEM observation of the consolidated Al_2O_3 film showed mechanical bonding between splatted Al_2O_3 particles and the sapphire substrate as well as mechanical bonding between the splatted Al_2O_3 particles themselves (difficult to identify splat boundaries). Moreover, each splatted particle became polycrystalline with 15-30nm nanocrystallites. We use the insight gained from these results to propose particle-substrate and particle-particle bonding mechanisms pertaining to systems where the ceramic particles (e.g. Al_2O_3) are deposited onto hard substrates, i.e. the substrates can support particle impact/deformation with minimal erosion (e.g. sapphire, zirconia, etc.). The mechanisms are schematically shown in Figure 31.

A. A single crystal particle travels towards the substrate at a velocity above the critical velocity for deposition.
B. The particle impacts the substrate. Assuming very little kinetic energy is converted to heat, as most kinetic energy is converted to absorbed strain energy during impact, which provides particle deformation and fracturing into nanocrystallites. The nanocrystallites are in intimate mechanical contact and chemi-mechanical bonds similar to grain boundaries are established between nanocrystallites and the substrate (especially for substrates of similar composition). The impacted particle remains together as a "splat" without fragmentation (28). The substrate beneath the particle is also deformed. The crystallites in the middle of the splat are chemi-mechanically bonded to the deformed substrate. However, at the particle edges, small gaps between the splat and the substrate remain.
C. A subsequent single crystal particle travels towards the pre-existing splat on the substrate at a velocity above the critical velocity for deposition. The particle impacts on the pre-existing splat and the substrate and undergoes the same deformation and bond formation processes described in B. However, the impacting particle imparts sufficient energy that the pre-existing splat and substrate are further deformed enabling further bond formation. This additional bond formation during the secondary particle impact creates the "tamping effect" described in the literature (40, 48-50).
D. The tamping effect closes gaps around the pre-exiting splat edges and allows complete mechanical bonding between the subsequent deformed/fractured particle and the pre-existing deformed/fractured splat. These processes are repeated multiple times, forming a consolidated film.

In this LDRD, we did not optimize the deposition process parameters to achieve thick consolidated films with high deposition efficiency. Also, while we demonstrated that Al_2O_3 can be deposited onto hard substrates such as sapphire and softer substrates such as silicon, we did not investigate the nature of the Al_2O_3 particle bonding on the softer substrates. We speculated that in the case where we deposited onto the softer substrate, the Al_2O_3 particles must first embed themselves in the soft substrate to create an anchor layer. Subsequent Al_2O_3 particles would exert a tamping effect, providing the energy to deform, fracture, and mechanically bond the arriving particles to the underlying embedded, anchored particles. We also speculated that lower particle velocity conditions should be used to achieve consolidated films on softer substrates because this will mitigate erosion of the anchoring layer.

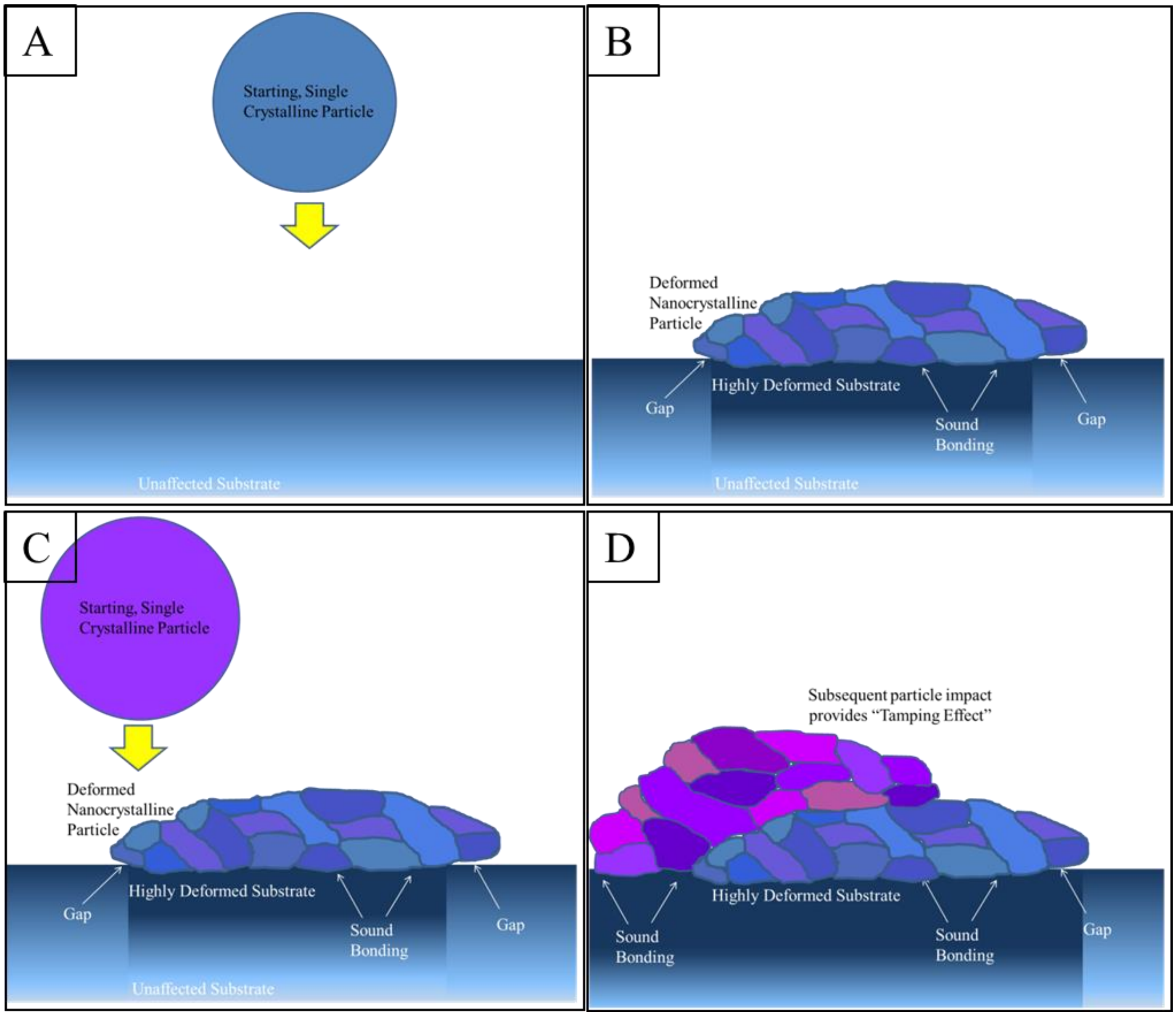

Figure 31: Proposed particle-substrate and particle-particle bonding mechanisms.

6.7. Key Points from Aerosol Deposition Studies

Particle velocity in the aerosol deposition process plays an important role in submicron particle deformation and film consolidation. Process parameters that can be adjusted to achieve desirable particle velocities include selecting the appropriate particle size and carrier gas type, as well as setting appropriate aerosol generation chamber pressure and standoff distance. Single particle deposition experiments showed that submicron alumina particles can impact, deform, change shape, and form crystallites without fragmentation, and will form an anchor layer mechanically bonding them to the substrate. The behavior of the impacting particles was very similar to the behaviors observed when submicron particles were subjected to quasi-static loading during the micro-compression experiments described in Section 4. The bonding between each splat and the substrate is complete near the middle of the splat whereas gaps remain around the splat edges. Alternatively, micron-sized alumina particles, fractured, fragmented, and dented the substrate. Coating deposition experiments strongly suggested that subsequent submicron alumina particles impacting the splatted anchor layer provided a “tamping effect”. The gaps around the splatted particles and the substrate were closed and bonding between the anchor layer and the substrate became complete. Subsequent coating buildup likely relies on the tamping effect to deform, fracture, and mechanically bond the arriving particles to the already deposited particles. Splat boundaries within the coatings were indistinguishable from grain boundaries. The consolidated Al_2O_3 coating is polycrystalline with 15-30nm nanocrystals. The coating preparation experiments reported here provide insights into adjusting process parameters to optimize coating deposition on various types of substrates.

7. RECOMMENDED FUTURE WORK

This LDRD provided proof of concept for submicron ceramic particle deformation and bonding to create consolidated ceramic coatings using the room temperature aerosol deposition process. The knowledge gained from this work provides a foundation to mature the aerosol deposition process for fabricating ceramic coatings on metallic, glass, and plastic substrates at room temperature. Considerable future work will be required to fully realize the potential of this unique coating deposition technique.

7.1. Changes to SNL Aerosol Deposition System

The current nozzle design is extremely efficient in achieving high velocity gas flows even at very low aerosol generation chamber pressures. This results in very high particle velocities even at lower carrier gas flow rates. While this nozzle was sufficient for our proof of concept work, it cannot achieve the range of particle velocities needed for process optimization; especially the lower velocities needed to deposit ceramics on soft substrates. We recommend designing a set of nozzles with varying geometries in order to cover a wide range of particle velocities and provide agility in future process optimization.

The current SNL aerosol deposition system was built to fit inside an existing and very large controlled atmosphere plasma spray chamber. Due to low deposition efficiency and no ability to recover the feedstock, a large amount of feedstock particles were consumed in the deposition process with very low return on coating thickness. While this was acceptable when spraying low cost Al_2O_3 feedstock, it would not be ideal for deposition of exotic, high cost feedstock materials. We recommend building a dedicated AD system and designing a built-in powder recovery process to minimize feedstock waste.

7.2. Process Maturation

Several key activities must be pursued to mature the AD process. First, process optimization to increase deposition efficiency must be performed. The influence of process parameters on coating microstructure and properties must be studied. Process parameters of interest include but are not limited to:

i. Feedstock particle material, size, and pre-treatment
ii. Substrate materials and substrate surface roughness
iii. Standoff distance and bow shock formation
iv. Carrier gas type and pressure
v. Deposition chamber pressure
vi. Stage traverse speed

The list of parameters includes factors such as i-ii related to feed and substrate properties and factors such as iii-vi which are related to controlling particle velocity. We suspect that these parameters govern the particle deformation, erosion, bonding, and coating properties.

The SNL 1-D code for particle velocity calculation can be helpful in understanding the process parameter effects on particle velocity. We recommend using CFD modeling in the future to understand the in-flight particle interaction with the chamber environment, to study bow shock effects in mild vacuum, and to better predict particle velocity at impact. We also recommend using laser Doppler velocimeter (LDV) (Figure 32) to compare/validate the measured 2-D particle velocity to the modeled particle velocity.

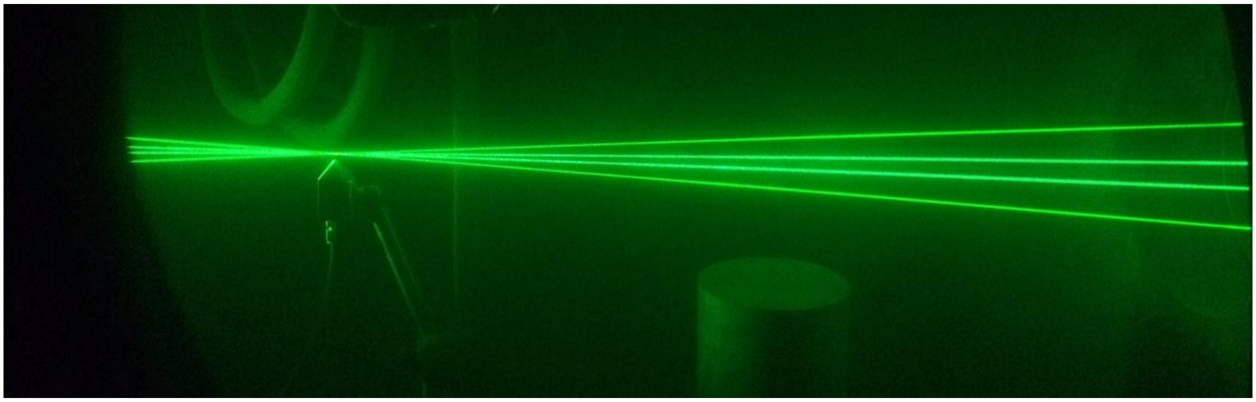

Figure 32: Laser beams used for laser Doppler velocimetry focused over the aerosol deposition nozzle and Al_2O_3 particle stream.

7.3. Feedstock Particle Preparation

We have proven in this LDRD that submicron particles capable of deformation must be used in the AD process to provide consolidation. We hypothesized that ball milling would introduce mobile dislocations in the particle interior, which are responsible for facilitating particle plastic deformation during impact (28). Less energy is required to move existing mobile dislocations as compared to nucleating new dislocations before moving them. This means ball milled particles that are full of mobile dislocations will be able to deform more easily and most likely at lower particle velocities during impact. Annealing ball milled particles to encourage polygonization—dislocation alignment to form subgrains—was shown to increase deposition efficiency in the AD process (40). We suspect that excessive annealing could result in defect recombination and dislocation annihilation, potentially lowering the particle deformability and resulting in lower deposition rates (28). However, we did not perform any experiments to investigate this. To prove this hypothesis, we recommend repeating the micro-compression experiments with particles that were ball-milled and annealed at different times to investigate the energy needed to further deform/fracture the pre-deformed particles. In addition, we recommend performing a series of experiments to investigate the effect of ball-milling, powder annealing, and calcination on deposition efficiency.

7.4. Measurement and Testing

Coating density as well as chemical and mechanical properties must be characterized. Defect density and crystallites morphology within deformed Al_2O_3 particles should be measured. Particle/particle interfaces, their orientations, boundary characteristics, chemical bonding, and phase content should be examined using SEM, TEM, and XRD. Coating hardness and fracture strength should also be determined. Residual stress must also be measured using micro-Raman Spectroscopy. This technique requires film thickness of >300 nm (thickness larger than the wavelength used). In addition, functional properties (dielectric, piezoelectric, paraelectric, thermal, thermomechanical, optical, magnetic, magneto-optical, etc.) should be investigated. For Al_2O_3, properties of interest may include dielectric permittivity, dielectric breakdown, thermal conductivity, thermal diffusivity, emissivity, etc. Ultimately, coating property measurement, microstructure characterization, and deposition process optimization must be done iteratively to achieve specific material properties for specific applications.

7.5. Film Annealing Treatment

As shown in the SEM and TEM images of Section 6, the as-deposited Al_2O_3 films are nanocrystalline with a grain size of 15-30nm. While these nanocrystalline grains contribute to higher strength and toughness for structural ceramics, larger grain size is needed to optimize other properties. We recommend exploring ex-situ and in-process coating annealing. Ex-situ film annealing can be done in a furnace to achieve residual stress relaxation and grain growth; although, the coefficient of thermal expansion mismatch and the structural integrity of the underlying substrate must be taken into account. The long term vision is to integrate an in-process annealing treatment with the deposition system but this could be difficult to achieve.

7.6. Modeling

As shown in Section 6, an existing particle laden flow model originally developed for calculating a 1-D particle velocity in cold and plasma spray processes was used to estimate AD particle velocities. The code takes into account nozzle geometry, gas type, inlet gas pressure, exit pressure, particle size, and particle properties (density, heat capacity, etc.). However, the code does not take into account the particle interaction with the vacuum environment in the deposition chamber or the particle interaction with the bow shock before the particle reaches the substrate. Thus the code is no longer once the particle exits the nozzle. We suggest using more sophisticated modeling tools such as CFD to understand particle interaction with the vacuum, the bow shock effect, and to predict particle velocity at impact.

In addition, more molecular dynamics simulation work should be performed to gain understanding of the particle-substrate interaction at impact. As shown in Section 6.3, we found in all cases studied to date, regardless of particle velocity or amount of viscous damping, that particles impacting single crystal substrates are reflected from the substrate without plastic deformation or adhesion, as seen in the experiments.

8. CONCLUSIONS

This LDRD proved submicron ceramic particles deform and bond in the aerosol deposition process at room temperature. Submicron ceramic particles capable of plastic deformation should be selected as feedstock for the aerosol deposition process. We showed submicron alumina particles can deform plastically (dislocation nucleation and slip) and fracture without fragmentation in quasi-static compressive loading at low strain rates. We also showed that high velocity impact can cause submicron alumina particles to deform, change shape without fragmentation, and adhere to the substrate as an anchor layer. Bonding between each splat and the substrate is present near the middle of the splat whereas gaps remain around the splat edges. Subsequent particles impacting on the splatted anchor layer likely produce a “tamping effect”. The gaps around the splatted particles and the substrate are closed and bonding between the anchor layer and the substrate becomes complete. Consequently, film buildup relies on the tamping effect to deform, fracture, and mechanically bond the arriving particles to the already deposited particles. The splat boundaries within the coatings were undistinguishable from other grain boundaries. The consolidated coating is polycrystalline with 15-30nm nanocrystals.

The knowledge gained from this work provides a strong foundation to mature the aerosol deposition process for fabricating ceramic films on metallic, glass, and plastic substrates at room temperature. Recommended future work is proposed around process optimization and understanding the process-microstructure-property relationships in aerosol deposited ceramic coatings.

9. REFERENCES

1. Imanaka Y, Hayashi N, Takenouchi M, Akedo J, "Technology for Embedding Capacitors on Printed Wiring Board Using Aerosol Deposition," Presented at Ceramic Interconnect and Ceramic Microsystems Technologies, 2006.
2. Imanaka Y, Hayashi N, Takenouchi M, Akedo J, "Aerosol deposition for post-LTCC," *J Euro Ceram Soc*, 2007, **27**, pp. 2789-95.
3. Akedo J and Ogiso H. " Room Temperature Impact Consolidation (RTIC) of Ceramic Fine Powder on Aerosol Deposition," Presented at 2nd International Conference and Exhibition on Ceramic Interconnect and Ceramic Microsystems Technologies, 2006.
4. Akedo J, "Room temperature impact consolidation (RTIC) of fine ceramic powder by aerosol deposition method and applications to microdevices," *JTST*, 2008, **17**, pp. 181-98
5. Kagotani T, Kobayashi R, Sugimoto S, Inomata K, Okayama K, Akedo J, "Magnetic properties and microwave characteristics of Ni-Zn-Cu ferrite film fabricated by aerosol deposition method," *J Magnetism Magnetic Mater*,2005, **290**, pp. 1442-45
6. Akedo J, "Aerosol deposition of ceramic thick films at room temperature: Densification mechanism of ceramic layers," *J Am Ceram Soc*, 2006, **89**, pp. 1834-39.
7. Kawakami Y, Yoshikawa H, Komagata K, Akedo J. " Powder preparation for 0.5 Pb(Ni1/3Nb2/3)O-3-0.15 PbZrO3-0.35PbTiO(3) thick films by the aerosol deposition method," *Journal of Crystal Growt*, 2005, **275**, pp. E1295-E300
8. Akedo J, Lebedev M, "Piezoelectric properties and poling effect of Pb(Zr, Ti)O-3 thick films prepared for microactuators by aerosol deposition," *Applied Physics Letters*, 2000, **77**, pp. 1710-12.
9. Exner J, Fuierer P, Moos R, "Aerosol Codeposition of Ceramics: Mixtures of Bi_2O_3-TiO_2 and Bi_2O_3-V_2O_5," *J Am Ceram Soc*, 2015, **98**, pp. 717-23
10. Sugimoto S, Maki T, Kagotani T, Akedo J, Inomata K, "Effect of applied field during aerosol deposition on the anisotropy of Sm-Fe-N thick films," *Journal of Magnetism and Magnetic Materials*, 2005, **290**, pp. 1202-05
11. Yamaguchi T, Shin KH, Lim PB, Uchida H, Inoue M, " PLZT films prepared by aerosol deposition and their birefringence evaluation," *IEEE Transactions on Electrical and Electronic Engineering*, 2007, **2**, pp. 458-62
12. Johnson SD, Glaser ER, Cheng SF, Kub FJ, Eddy CR. "Characterization of as-deposited and sintered yttrium iron garnet thick films formed by aerosol deposition," *Applied Physics Express* 2014, **7**, pp. 035501-4.
13. Chun DM, Ahn SH. " Deposition mechanism of dry sprayed ceramic particles at room temperature using a nano-particle deposition system," *Acta Materialia*, 2011, **59**, pp. 2693-703
14. Park H, Kwon J, Lee I, Lee C, "Shock-induced plasticity and fragmentation phenomena during alumina deposition in the vacuum kinetic spraying process." *Scripta Materialia*, 2015, **100**, pp. 44-47.
15. Imanaka Y, Amada H, Kumasaka F, Takahashi N, Yamasaki T, et al. "Nanoparticulated Dense and Stress-Free Ceramic Thick Film for Material Integration," *Advanced Engineering Materials*, 2003, **15**, pp.1129-1135.
16. Ruano OA, Wadsworth J, and Sherby OD, "Deformation of fine-grained alumina by grain boundary sliding accommodated by slip," *Acta Mater*. 2003, **51**, pp. 3617-3634.

17. Dominguez-Rodriguez A, Gutierrez-Mora F, Jimenez-Melendo M, Routbort JL, and Chaim R, "Current understanding of superplastic deformation of Y-TZP and its application to joining," *Mater. Sci. Engr. A*. 2001, **302**, pp. 154-161.
18. Montagne S, Pathak S, Maeder X, and Michler J, "Plasticity and fracture of sapphire at room temperature: load-controlled microcompression of four different orientations," *Ceram Int*., 2014, **40**, pp. 2083-2090.
19. Beaber AR, *et al*., "Smaller is Tougher," *Philos. Mag*., 2011, **91**, pp. 1179-1189.
20. Gerberich WW, *et al*., "Scale Effects for Strength, Ductility, and Toughness in "Brittle" Materials," *J. Mater. Res*., 2009, **24**, pp. 898-906.
21. Gerberich WW, *et al.*, "Reverse Plasticity in Single Crystal Silicon Nanospheres," *Int J Plasticity*., 2005, **21**, pp. 2391-2405.
22. Ostlund F, *et al*., "Brittle-to-Ductile Transition in Uniaxial Compression of Silicon Pillars at Room Temperature," *Adv. Funct. Mater*., 2009, **19**, pp. 2439-2444.
23. Xu G and Zhang C., "Analysis of Dislocation Nucleation from a Crystal Surface Based on the Peierls-Nabarro Dislocation Model," *J. Mech. Phys. Solids*, 2003, **51**, pp. 1371-1394.
24. Howie PR, *et al.*, "Fracture Modes in Micropillar Compression of Brittle Crystals," *J. Mater. Res.*, 2012, **27**, pp. 141-151.
25. Mook WM, *et al.*, "Compression of Freestanding Gold Nanostructures: From Stochastic Yield to Predictable Flow," *Nanotechnology*, 2010, **21**, pp. 055701-9.
26. Bei H, *et al.*, "Effects of Pre-Strain on the Compressive Stress-Strain Response of Mo-Alloy Single-Crystal Micropillars," *Acta Mater*., 2008, **56**, pp. 4762-4770.
27. Ostlund F, *et al*., "Ductile-Brittle Transition in Micropillar Compression of GaAs at Room Temperature," *Philos. Mag*. 2011, **91**, pp. 1190-1199.
28. Sarobol P, *et al*., "Room Temperature Deformation Mechanisms of Alumina Particles Observed from In Situ Micro-compression and Atomistic Simulation," *JTST*, 2016, **25**, pp. 82-93.
29. Blonski S and Garofalini SH, "Molecular Dynamics Study of Silica-Alumina Interfaces," *J. Phys. Chem*., 1996, **100**, p. 2201-2205.
30. Litton AD and Garofalini SH, "Modeling of Hydrophilic Wafer Bonding by Molecular Dynamics Simulations," *J. Appl. Phys*., 2001, **89**, p. 6013-6023.
31. Tymiak NI and Gerberich WW, "Initial stages of contact-induced plasticity in sapphire. I. Surfaces traces of slip and twinning," *Phil. Mag*., 2007, **87**, p. 5143-5168.
32. Tymiak NI and Gerberich WW, "Initial stages of contact-induced plasticity in sapphire. II. Mechanisms of plasticity initiation," *Phil. Mag*., 2007, **87**, p. 5169-5188.
33. Nowak R, Sekino T, and Niihara K, "Surface deformation of sapphire crystal," *Phil. Mag. A*, 1996, **74**, p. 171-194.
34. Clayton JD, "A continuum description of nonlinear elasticity, slip and twinning, with application to sapphire," *Proc. Of the Royal Soc. A.*, 2009, **465**, p. 307-344.
35. Dobrovinskaya ER, Lytvynov LA, and Pishchik V, "Properties of Sapphire," *Sapphire*, Springer, Boston, MA, US, 2009.
36. Hysitron I SEM Picoindenter User Manual. Revision 9.3.0913 edn. 2013.
37. *Materials Science and Engineering Serving Society* edited by Chang RPH, Roy R, Doyama M, and Somiya S. (Elsevier Science, The Netherlands, 1998).
38. Sarobol P, *et al*., "Additive Manufacturing of Hybrid Circuits," *Annual Review of Materials Research*, 2016, **46**.

39. Akedo J, Lebedev M, " Powder preparation in aerosol deposition method for lead zirconate titanate thick films." *Japanese Journal of Applied Physics Part 1-Regular Papers Short Notes & Review Papers* 2002, **41**, pp. 6980-84.
40. Park H, Heo J, Cao F, Kwon J, Kang K, Bae G, and Lee C, "Deposition Behavior and Microstructural Features of Vacuum Kinetic Sprayed Aluminum Nitride," *JTST*, 2013, **22**, pp. 882-891.
41. Schubert M, Exner J, Moos R. "Influence of Carrier Gas Composition on the Stress of Al_2O_3 Coatings Prepared by the Aerosol Deposition Method," *Materials*, 2014, **7**, pp. 5633-42.
42. Inoue M, Mitzoguchi M, Lim PB, Uchida H, and Shin KH, "Preparation of Thick Magnetic Garnet Films with Aerosol Deposition Method and their Magnetic Properties," Proceeding of the 2nd International Conference and Exhibition on Ceramic Interconnect and Ceramic Microsystems Technologies, CICMT 2006.
43. Furuta T, Hatta S, Kigoshi Y, Hoshina T, Takeda H, Tsurumi T. Dielectric Properties of Nanograined BaTiO3 Ceramics Fabricated by Aerosol Deposition Method. *Electroceramics in Japan Xi,* 2011, **485**, pp. 183-86
44. Dykhuizen RC and Smith MF, "Gas Dynamic Principles of Cold Spray," *JTST*, 1997, **7**, pp. 205-212.
45. Dykhuizen RC, Smith MF, Gilmore DL, Neiser RA, Jian X, and Sampath S, "Impact of High Velocity Cold Spray Particles," *JTST*, 1999, **8**, pp. 559-564.
46. Gilmore D., Dykhuizen RC, Neiser RA, Roemer TJ, and Smith MF, "Particle Velocity and Deposition Efficiency in the Cold Spray Process," *JTST*, 1999, **8**, pp. 576-582.
47. Pitman MC and van Duin ACT, "Dynamics of Confined Reactive Water in Smectic Clay–Zeolite Composites." *Journal of the American Chemical Societ*y, 2012, **134**, 3042-3053.
48. Wang Y-Y, Liu Y, Yang G-J, Feng J-J, and Kusumoto K., "Effect of Microstructure on the Electrical Properties of Nano-Structured TiN Coatings Deposited by Vacuum Cold Spray," *JTST*, 2010, **19**, pp. 1231-1237.
49. Cao F, Park H, Heo J, Kwon J, and Lee C, "Effect of Process Gas Flow on the Coating Microstructure and Mechanical Properties of Vacuum Kinetic-Sprayed TiN Layers," *JTST*, 2013, **22**, pp. 1109-1119.
50. Fan S-Q, Yang G-J, Li C-J, Liu G-J, and Zhang L-Z, "Characterization of Microstructure of Nano-TiO_2 Coating Deposited by Vacuum Cold Spraying," *JTST*, 2006, **15**, pp. 513-517.

DISTRIBUTION

1	MS0359	Donna L. Chavez	01911
1	MS0885	Mark Smith	01801
1	MS0886	Paul Kotula	01819
1	MS0889	Michael Chandross	01814
1	MS0959	Deidre Hirschfeld	01832
1	MS1086	Robert Biefeld	01120
1	MS1130	Aaron Hall	01832
1	MS1130	Pylin Sarobol	01832
1	MS0899	Technical Library	09536 (electronic copy)

Sandia National Laboratories